

The Open University's repository of research publications
and other research outputs

Human-assisted Sample Return Mission at the Schrödinger Basin, Lunar Far Side, Using a New Geologic Map and Rover Traverses

Journal Item

How to cite:

Czaplinski, E. C.; Harrington, E. M.; Bell, S. K.; Tolometti, G. D.; Farrant, B. E.; Bickel, V. T.; Honnibal, C. I.; Martinez, S. N.; Rogaski, A.; Sargeant, H. M. and Kring, D. A. (2021). Human-assisted Sample Return Mission at the Schrödinger Basin, Lunar Far Side, Using a New Geologic Map and Rover Traverses. *The Planetary Science Journal*, 2(2), article no. 51.

For guidance on citations see [FAQs](#).

© 2021 E. C. Czaplinski; 2021 E. M. Harrington; 2021 S. K. Bell; 2021 G. D. Tolometti; 2021 B. E. Farrant; 2021 V. T. Bickel; 2021 C. I. Honnibal; 2021 S. N. Martinez; 2021 A. Rogaski; 2021 H. M. Sargeant; 2021 D. A. Kring



<https://creativecommons.org/licenses/by/4.0/>

Version: Version of Record

Link(s) to article on publisher's website:
<http://dx.doi.org/doi:10.3847/psj/abdb34>

Copyright and Moral Rights for the articles on this site are retained by the individual authors and/or other copyright owners. For more information on Open Research Online's data [policy](#) on reuse of materials please consult the policies page.



Human-assisted Sample Return Mission at the Schrödinger Basin, Lunar Far Side, Using a New Geologic Map and Rover Traverses

E. C. Czaplinski¹ , E. M. Harrington² , S. K. Bell³ , G. D. Tolometti⁴ , B. E. Farrant³ , V. T. Bickel^{5,6} ,
C. I. Honniball^{7,13} , S. N. Martinez⁸ , A. Rogaski⁹, H. M. Sargeant¹⁰ , and D. A. Kring^{11,12}

¹ Arkansas Center for Space and Planetary Sciences, University of Arkansas, USA; eczapli@uark.edu

² Centre for Earth Evolution and Dynamics, Department of Geosciences, University of Oslo, Oslo, Norway

³ Department of Earth and Environmental Science, University of Manchester, Manchester, UK

⁴ Department of Earth Sciences, University of Western Ontario, London, Ontario, Canada

⁵ Department Planets & Comets, Max Planck Institute for Solar System Research, Göttingen, Germany

⁶ Department of Earth Sciences, Swiss Federal Institute of Technology Zurich, Zurich, Switzerland

⁷ NASA Goddard Space Flight Center, Greenbelt, MD, USA

⁸ Department of Earth and Environmental Sciences, Tulane University, New Orleans, LA, USA

⁹ Department of Geology and Geological Engineering, South Dakota School of Mines and Technology, Rapid City, SD, USA

¹⁰ School of Physical Sciences, The Open University, Milton Keynes, UK

¹¹ Center for Lunar Science and Exploration, Lunar and Planetary Institute, USRA, Houston, TX, USA

¹² NASA Solar System Exploration Research Virtual Institute, Houston, TX, USA

Received 2020 October 2; revised 2021 January 7; accepted 2021 January 11; published 2021 March 12

Abstract

The Schrödinger basin on the south polar lunar far side has been highlighted as a promising target for future exploration. This report provides a high-resolution geologic map in the southwest peak-ring (SWPR) area of the Schrödinger basin, emphasizing structural features and detailed mapping of exposed outcrops within the peak ring. Outcrops are correlated with mineralogical data from the Moon Mineralogical Mapper instrument. Geologic mapping reveals a complex structural history within the basin through a system of radially oriented faults. Further, the geologic map shows both faulted and magmatic contacts between peak-ring mineralogies, providing both structural and magmatic context for understanding lunar crustal evolution and polar region processes. To investigate these relationships and address key scientific concepts and goals from the National Research Council (NRC) report, we propose three traverse paths for a robotic sample return mission in the SWPR area. These traverses focus on addressing the highest priority science concepts and goals by investigating known outcrops with diverse mineralogical associations and visible contacts among them. Coinciding with the preparation for the 2024 Artemis III mission, NASA is increasing the priority of robotic exploration at the lunar south pole before the next crewed mission to the Moon. Through mapping the Schrödinger SWPR, we identified the extent of different lunar crustal mineralogies, inferred their geologic relationships and distribution, and pinpointed traversable routes to sample spectrally diverse outcrops and outcrop-derived boulders. The SWPR region is therefore a promising potential target for future exploration, capable of addressing multiple high-priority lunar science goals.

Unified Astronomy Thesaurus concepts: [The Moon \(1692\)](#); [Lunar science \(972\)](#); [Selenology \(1441\)](#); [Lunar surface \(974\)](#)

1. Introduction

On the Moon, the Schrödinger basin is the second youngest impact basin residing within the oldest, the South Pole–Aitken basin (Figure 1). Schrödinger is a 320 km diameter impact basin and contains a 150 km peak-ring structure ranging in elevation from 1 to 2.5 km above the basin floor. A previous study of lunar landing sites (Kring & Durda 2012) revealed that the Schrödinger basin is a high-priority site for future missions, because more of the science objectives identified for NASA (National Research Council 2007, hereafter NRC 2007) can be accomplished there than at any other location on the Moon. For that reason, several studies of potential landing sites within the Schrödinger basin and notional traverses, both for robotic and

crew assets, have been produced (Bunte et al. 2011; O’Sullivan et al. 2011; Potts et al. 2015; Steenstra et al. 2016).

In previous studies, mapping the Schrödinger basin was conducted as part of a south polar mapping project that utilized Lunar Orbiter photographs (Wilhelms et al. 1979). The basin was re-examined using Clementine (Shoemaker et al. 1994) and Lunar Reconnaissance Orbiter (Mest 2011; Kramer et al. 2013; Fortezzo et al. 2020) data. Based on these previous studies, surface units within the Schrödinger basin were divided into three assemblages, according to their origin. These are the volcanic formation (low-albedo mantling and plains materials), plains formation (non-volcanic plains materials with various albedos and textures), and basin materials (including peak-ring, rim, and well-preserved crater material; Shoemaker et al. 1994). Four distinct mineralogic units have been identified (Kramer et al. 2013) in Schrödinger’s peak-ring structure using spectral reflectance data from the Moon Mineralogy Mapper (M³) on the Chandrayaan-1 spacecraft. The M³ data have been used to infer anorthositic (An), pyroxene-bearing anorthositic (Pb), noritic (No), and troctolitic (Tr) mineralogical signatures, which are interpreted to represent mineralogies of those types.

¹³ NASA Postdoctoral Program Fellow.



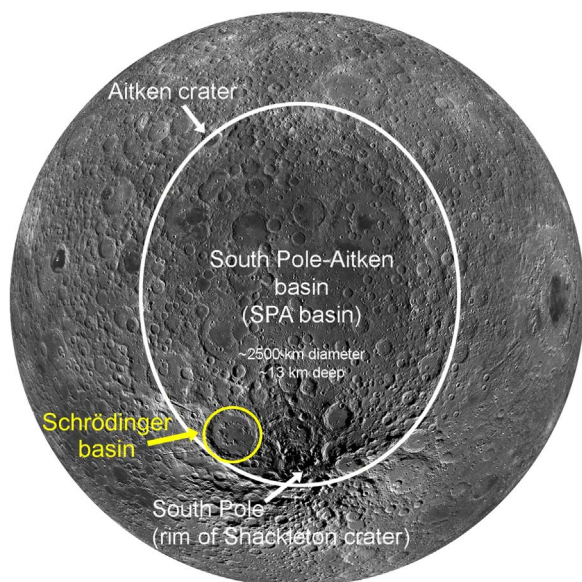


Figure 1. View of the southern, midlatitude far side of the Moon showing the SPA basin outlined in white and the Schrödinger basin outlined in yellow (modified from LPI Lunar South Pole Atlas).

The diversity of lunar crustal rocks and their distribution in the Schrödinger basin is one of the top 10 outstanding lunar science goals (NRC 2007). Anorthosite, pyroxene-bearing anorthosite, norite, and troctolite are all intrusive igneous rocks that form within the lunar crust. Each rock type is defined by its relative abundances of the minerals plagioclase, pyroxene, and olivine. Anorthosite consists almost entirely of plagioclase (>90%) with small amounts of pyroxene or olivine. The anorthositic crust has been hypothesized to be a product of a crystallized lunar magma ocean, from the floatation of plagioclase crystals rising to the surface to form a primordial crust (Wood et al. 1970). This is the most accepted hypothesis in the lunar community, although new studies have proposed that the anorthositic crust may represent a primordial crust that was metasomatized by incompatible element KREEP melt and mantle partial-melt material (Xu et al. 2020). Rocks that contain more clinopyroxene (>10%–90%) but neither orthopyroxene nor olivine are norite (Prinz & Keil 1977; Stöffler et al. 1980). Lunar norite is interpreted as a plutonic igneous rock that has been uplifted from beneath the lunar crust (Shih et al. 1993). Norite clasts analyzed in Apollo impact breccias reveal plutonic petrographic textures and isotopic signatures (Dymek et al. 1975), but the true petrogenesis is unknown due to impact-cratering processes. Rocks whose pyroxene abundance lies along the anorthosite–norite boundary are referred to as pyroxene-bearing anorthosite, and these can be inferred through a unique spectral signature (Kramer et al. 2013). Finally, troctolite is composed of plagioclase and olivine, without pyroxene (Prinz & Keil 1977; Stöffler et al. 1980). Troctolite is thought to have originated from the deepest parts of the lunar crust and potentially the upper mantle (Kring et al. 2016). Numerical modeling by Kring et al. (2016) estimates that material may have been uplifted from depths as low as 15 to 26 km. Therefore, these rocks are of great importance for answering the high-priority science goals of the NRC (2007) report concerning the formation of the lunar surface.

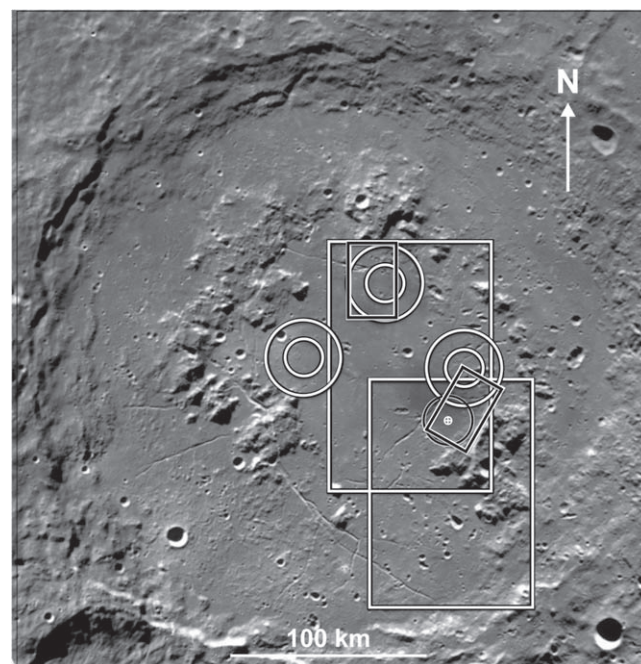


Figure 2. Locations of the O’Sullivan et al. (2011; three white circles), Potts et al. (2015; two small black rectangles), Steenstra et al. (2016; two large white rectangles), and Bunte et al. (2011; small black circle) traverse regions in the Schrödinger basin. Potts et al. (2015) proposed two 14 day robotic missions in the pyroclastic and mare deposits, and Steenstra et al. (2016) focused on covering much of the central and southern regions of the Schrödinger basin to maximize sample return diversity from robotic missions. The landing sites and crewed traverses proposed by O’Sullivan et al. (2011) were designed for astronauts performing extravehicular activities EVAs up to ~22 hr. Bunte et al. (2011) present four crewed EVAS over the course of 4 days, which allow for detailed analysis of pyroclastic vent samples.

The Schrödinger basin hosts a variety of geological features that are capable of addressing most NRC (2007) science concepts and goals (O’Sullivan et al. 2011; Kring & Durda 2012; Potts et al. 2015; Steenstra et al. 2016). On the floor of the basin is a large impact melt sheet (Kramer et al. 2013) that is vital for addressing the top three NRC (2007) science goals, as it can date the age of the impact basin and constrain the timing of the inner solar system bombardment history. Additional NRC (2007) report scientific goals can be addressed by a diverse assortment of pyroclastic deposits (Shoemaker et al. 1994; Mest 2011; Steenstra et al. 2016), partially shadowed regions that may host dispersed water ice and other volatile-rich regolith (e.g., Li et al. 2018; Honniball et al. 2021), secondary craters, and uplifted peak-ring lithologies that have been identified within the Schrödinger basin through orbital mapping.

Three previous studies evaluated potential future landing sites in the central and southern regions of the Schrödinger basin, and two of the studies designed traverse paths for 14 day and 3–4 yr long missions (Figure 2; O’Sullivan et al. 2011; Potts et al. 2015; Steenstra et al. 2016). These two missions use the NASA Orion spacecraft and HERACLES concept developed by the European Space Agency (ESA) to teleoperate a rover on the surface of the Moon in real time. Both studies selected landing sites on the dark mantle deposits (i.e., likely pyroclastics) in the central-east region of Schrödinger, in part, to sample material suitable for in situ resource utilization on the Moon. Rover traverses from those landing sites focused on the

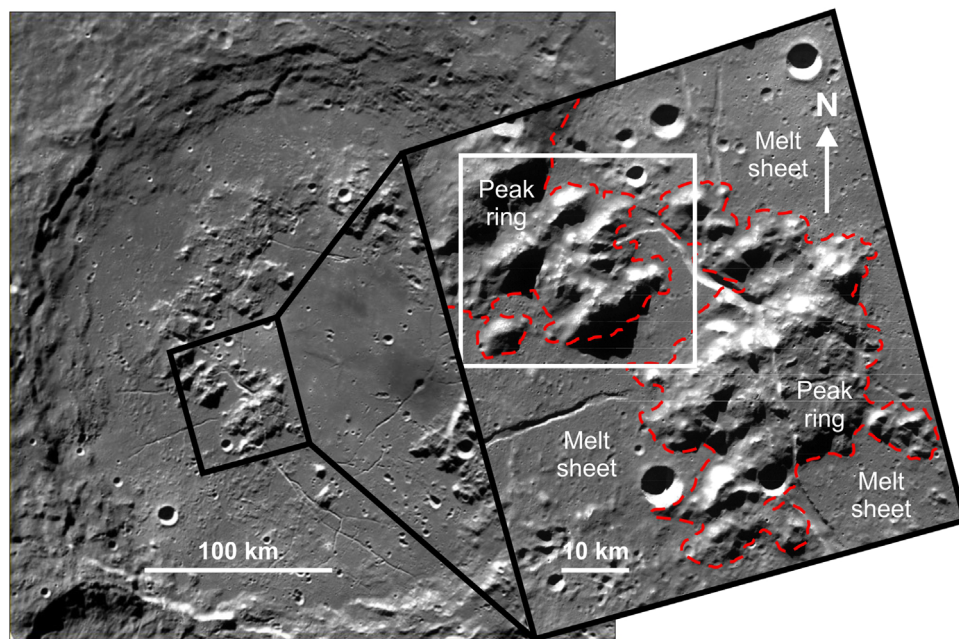


Figure 3. WAC mosaic image of the Schrödinger basin (left) with a zoomed-in view of the SWPR area (right; the study area of this work) including labeled impact melt sheet and the peak ring outlined in red. The inset white box outlines the study area from Kring et al. (2016).

northern and eastern sides of the basin, near the prominent pyroclastic vent (Hurwitz & Kring 2015; Potts et al. 2015; Steenstra et al. 2016). A series of recent studies have shown that proposed traverses across the various terrain types within Schrödinger (pyroclastics, shadowed regions, etc.) and across south polar regions are feasible from a trafficability point of view (Bickel et al. 2019; Bickel & Kring 2020; Sargeant et al. 2020).

Sampling outcropped material provides some of the highest scientific potential for understanding the context of the peak-ring mineralogies. Work by Kramer et al. (2013) revealed pyroxene-bearing anorthosite exposures in Schrödinger’s southern walls that have been interpreted as material excavated during the Schrödinger basin-forming event. Additionally, the composition of Schrödinger’s peak ring, as outlined in Kramer et al. (2013), indicates that the large blocks of exposed material may be left over from the lunar magma ocean. Multi-kilometer-long outcrops of crystalline lithologies shown in Kring et al. (2017) highlight incredible opportunities to study Schrödinger’s peak-ring mineralogy up close. Therefore, Schrödinger offers an excellent location for sample return missions and robotic exploration of a high-priority target that provides many chances to address major NRC (2007) exploration concepts.

Here, we build upon the work of Kramer et al. (2013) and Kring et al. (2016) by mapping the spectrally and structurally diverse southwest peak-ring (SWPR) area (Figure 3) in greater detail at an outcrop scale (1:300,000). This mapped area contains four main spectral units and is used to design three possible human-assisted robotic traverse paths for a sample return mission, which are optimized for diverse sample collection within a single lunar day.

This effort may be particularly timely, because NASA has selected the floor of the Schrödinger impact basin as the landing site for the second quarter of 2024 using a Commercial Lunar Payload Services contract. While the mission will not

likely be a sample return mission, the geology represented in the mapping here may help to refine options for that mission.

2. MAPPING: Data and Rationale

Craters, ejecta, talus, faults, and outcrop exposures were mapped separately throughout the SWPR before being merged into a final map. This approach ensures that the features were mapped continuously across multiple mapped sections. The geological features were mapped individually in Java Mission-planning and Analysis for Remote Sensing (JMARS; Christensen et al. 2009) as custom-shape layers (polygons, polylines, and point features), and included craters and ejecta, outcrops, structural features (faults and graben), talus, and low-albedo features. The selection criteria for each feature type can be found in Appendix A.

2.1. Data Sets for the Map

The geologic map was produced using a combination of different remote-sensing data sets over the SWPR area in the Schrödinger basin. The data come from multiple instruments and preexisting maps, including the Clementine Ultraviolet/Visible camera (UVVIS; Bussey & Spudis 2004), the Lunar Reconnaissance Orbiter (LRO) Wide-Angle Camera (WAC) and Narrow-Angle Camera (NAC; Robinson et al. 2010), the Lunar Orbiter Laser Altimeter (LOLA) (Smith et al. 2010), the Miniature Radio Frequency (Mini-RF) instrument (Nozette et al. 2010), the Kaguya Spectral Profiles (from the SELENE mission; Ohtake et al. 2008), M³ data (Green et al. 2011), and geological maps created by Kramer et al. (2013) and Kring et al. (2016). These images and data sets were analyzed via the LROC Quickmap and Moon Trek websites and the ArcGIS and JMARS software. The final products were uploaded in ArcGIS 10.3.1 to construct geologic maps of the SWPR. New LRO NAC data strips were downloaded from the Planetary Data System and converted to images readable in ArcGIS using the

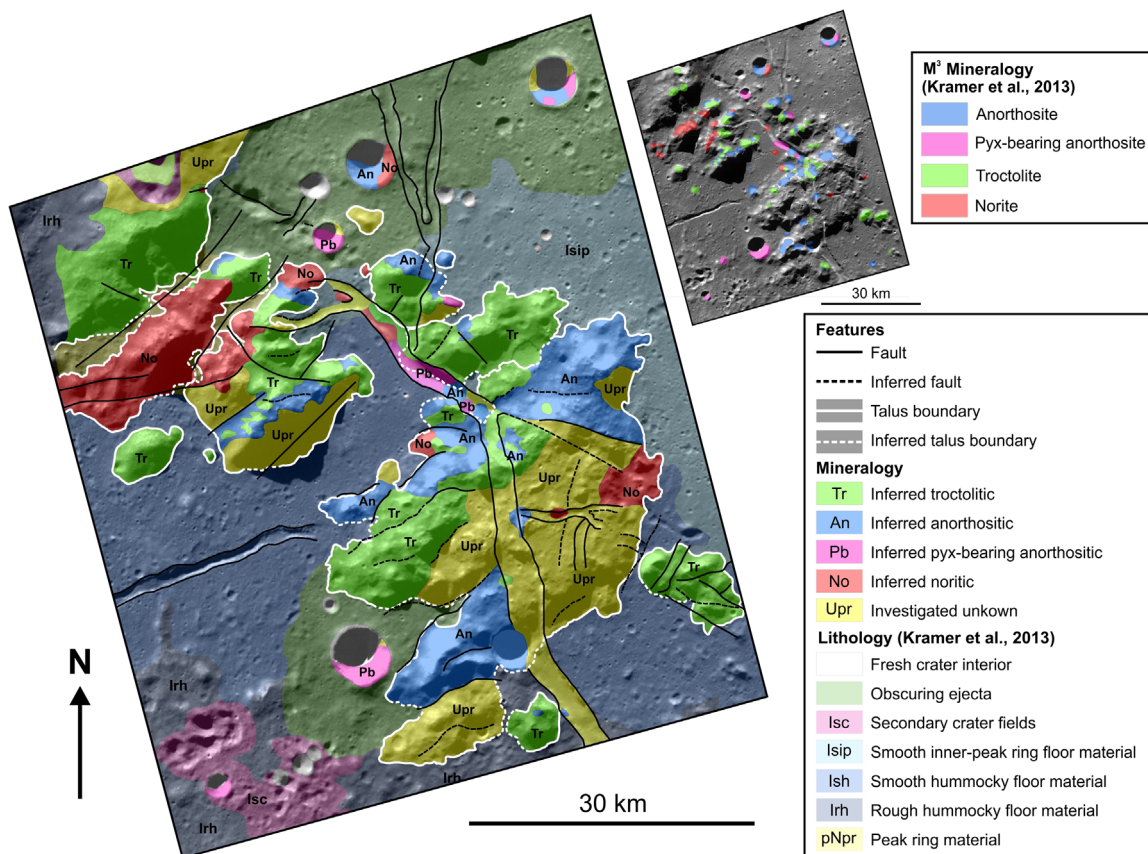


Figure 4. Geologic map of the SWPR, including structural features, geologic units outlined in Kramer et al. (2013; upper-right inset), and inferred lithologies in the peak ring.

USGS Integrated Software for Imagers and Spectrometers (ISIS3) program. The kernels were added (spiceinit) to each image before calibration and map projection.

2.2. Mapping Limitations

The mapping resolution is limited by available orbital data. As discussed by Kramer et al. (2013), the high-latitude location of the Schrödinger basin is not ideal for imaging spectroscopy, so meaningful spectra are limited to a few locations, mostly on reflective slopes like those on the peak ring and crater walls. Some of those locations occur on outcrops exposed along the ridges of the large, radially oriented faulted blocks. Outcrops were also more readily identified on the north-facing side of ridges due to trends in surface illumination for these areas, as north-facing ridges are better lit during the lunar day than south-facing ridges. Consequently, most outcrop exposures covered by M³ data are found in crater walls and on the walls of uplifted peak-ring material. This limitation is also reflected in the large areas labeled “investigated unknown.”

3. Mapping Results

Using the imagery and spectral data described in Section 2.1, each feature was identified manually using the highest resolution imagery available in either JMARS or ArcGIS software. In total, we marked 1586 separate shapefile features (1238 boulder fields, 190 fresh craters, 64 rille boundaries, 37 regolith boundaries, 33 shadowed areas with potential volatiles, 17 outcrops, 4 low-albedo features, and 3 secondary craters) within the SWPR mapping region (Figure A7). Several

individual maps in Appendix A (Figures A1–A7) are available, each highlighting different feature types. These new data are combined with M³ mapping from Kramer et al. (2013) to infer the composition of exposed outcrops in the SWPR. We created a full geologic map of the SWPR area, shown in Figure 4, by combining all mapped structural features (Figure A5) and the mapped inferred lithologies of the peak-ring material (Figure A6), with the Schrödinger basin floor lithologies mapped by Kramer et al. (2013). The map shown in Figure 4 covers an area of ~5350 km², at a scale of 1:300,000, providing a detailed view of the mineralogy present within the peak-ring material.

The exposed peak-ring material is inferred as troctolitic, anorthositic, pyroxene-bearing anorthositic, or noritic based on available M³ data (Kramer et al. 2013). The talus boundary marks the transition between peak-ring mineralogies and Schrödinger basin floor material. Regions designated as “investigated unknown” represent areas that could not be reliably assigned a mineralogy due to lack of M³ data and poor surface illumination. There is no reason to suspect that regions of investigated unknowns would not be identifiable as one of the four peak-ring mineralogies, if additional data become available.

Peak-ring material is concentrated in two main uplifted regions: a smaller NW region and a larger SE region. Troctolitic and anorthositic materials are inferred to be the two most common mineralogies in the SWPR by area (excluding investigated unknown). Troctolitic outcrops are concentrated at topographic highs, such as peaks of hills and mounds within the SWPR. Anorthositic outcrops are spread

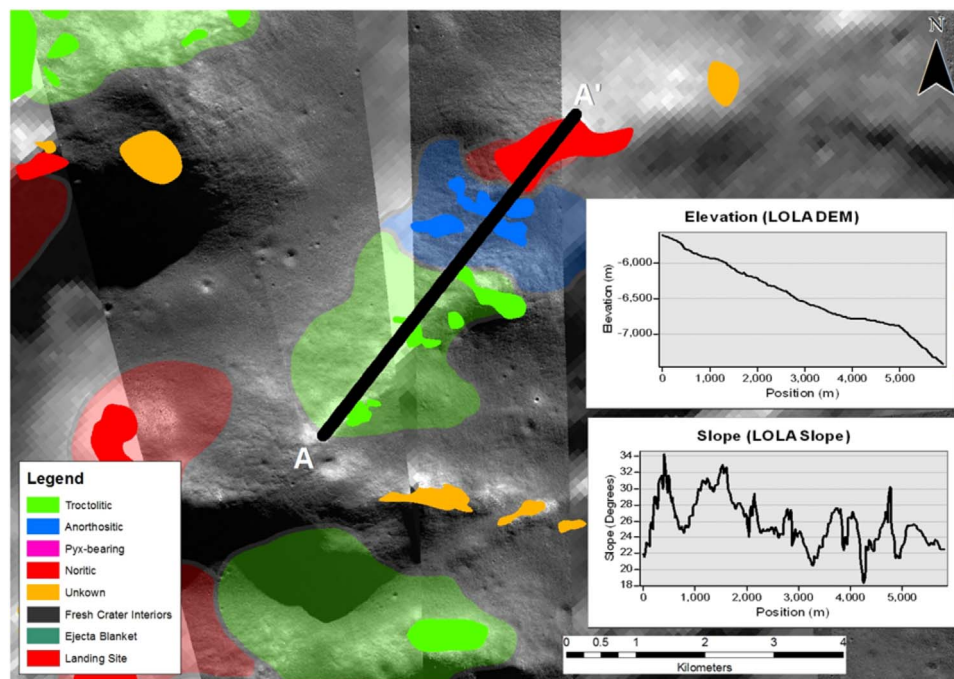


Figure 5. Elevation and slope profiles drawn using ArcGIS were used to identify topographical and slope changes among M^3 signatures. Changes in topography may indicate a faulted contact, while no change may indicate a magmatic contact (NAC image IDs: M1105154228LC, M110779249LC, M189749586LC).

throughout the entire SWPR, with the largest concentrations in the SE region. The largest exposure of noritic outcrops is concentrated in the NW region of the SWPR. There are also several smaller noritic regions in the SE portion of the SWPR. Pyroxene-bearing anorthositic material is the least exposed of the SWPR mineralogies, and outcrops are predominantly limited to topographic lows (e.g., craters and graben), where the subsurface is exposed.

Mapping the SWPR area of the Schrödinger basin revealed complex faulting associated with basin formation. Numerous faults were found within the uplifted regions of peak-ring material. Several graben were also identified both within the peak-ring and basin-floor material, including a 2.5 km wide, N–S trending graben that runs through the SE portion of the peak ring.

3.1. Key Findings

3.1.1. Magmatic versus Faulted Contacts

To address outstanding questions about the lunar crust, we investigated whether the contacts between mineralogies in the SWPR are magmatic or structural (faulted) in origin. Faulted contacts provide information on peak-ring formation processes and the forces and processes involved in uplifting material from a depth within the lunar crust (e.g., Kring et al. 2016). Observations of faulted contacts within the SWPR would help address many of the science goals within NRC (2007) concept 6, with regard to impact processing on a planetary scale. Equally important, magmatic contacts provide information about the nature of the lunar crust and the magmatic processes operating during its formation (e.g., Pernet-Fisher & Joy 2016). Observations of any magmatic contacts within the SWPR would help address many of the high-priority goals within NRC (2007) concept 2 regarding the composition and structure of the lunar interior.

Identifying visible contacts among spectral units is challenging because regolith, talus, high-albedo slopes, and shadows cover most of the SWPR area. Our criteria for proposed faults and magmatic contacts rely on inferred slope breaks or lack thereof (e.g., Figure 5). As previously described (Kring et al. 2016), there are no erosional processes on the Moon that carve sharp valleys in mountains; however, localized granular flow gullies and landslides in fresh craters within the Schrödinger basin are an example of surficial erosion (Kumar et al. 2013). Thus, we interpret that differential topography in the peak ring was created by faults (Figure 6). Faulted contacts are identified when features cross-cut mineralogical boundaries or parallel mineralogical boundaries. On the other hand, mineralogical boundaries without any topographic expression may, instead, be magmatic contacts. While we cannot rule out the possibility that those contacts are faulted, they are mapped as magmatic contacts here.

In the NW portion of the peak ring, noritic exposures display predominantly faulted contacts with other mineralogies, and noritic outcrops are found within large, homogenous fault-bounded blocks (Figure 7, #1). However, smaller exposures of noritic mineralogies have been interpreted as being in magmatic contact with other peak-ring mineralogies, particularly at the base of mounds, in fresh craters, and in the wall of the N–S trending graben (Figure 7).

Pyroxene-bearing anorthosite has been interpreted as being the only rock type that solely exhibits magmatic contacts with other mineralogies (Figure 7). However, it is difficult to make inferences based on the occurrence of pyroxene-bearing anorthositic mineralogy, due to the complex nature of the SWPR and its relatively low abundance. As outcrops are predominantly limited to the SW wall of the graben (Figure 7, #2) and within fresh craters, one possibility is that the pyroxene-bearing anorthositic signatures represent the exposed melt sheet (Kramer et al. 2013).

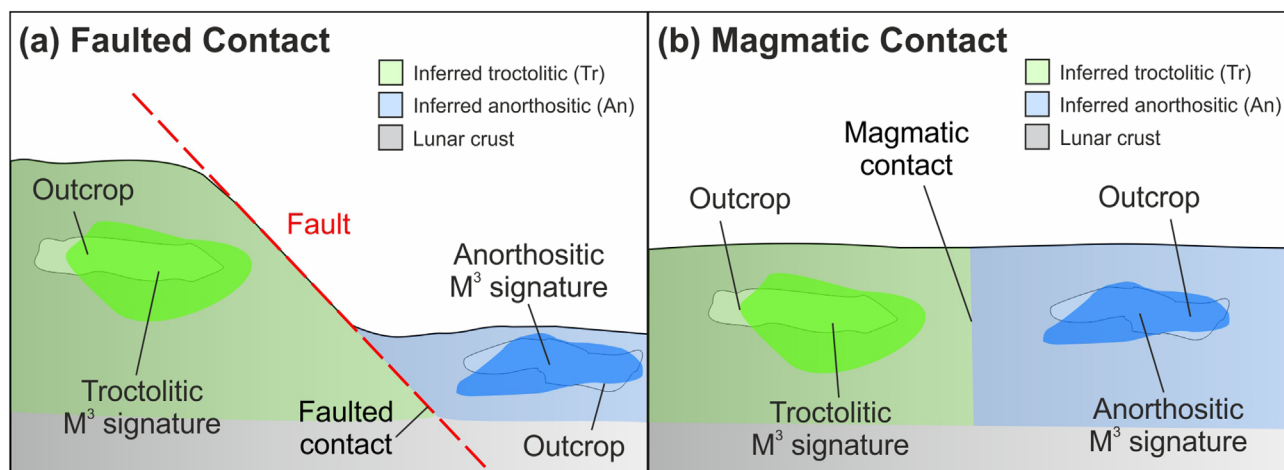


Figure 6. Cross-section view of proposed nature of contacts between the outcrops in the Schrödinger basin on the Moon. (a) Changes in topography between outcrops from structural geological processes, such as faults, are interpreted as faulted contacts. (b) A lack of topographical change between two outcrops of different mineralogies is interpreted to be magmatic in origin. This is a simplified schematic of these types of contacts, as they can occur in more complicated orientations than shown, (e.g., more than one fault separating the faulted contacts).

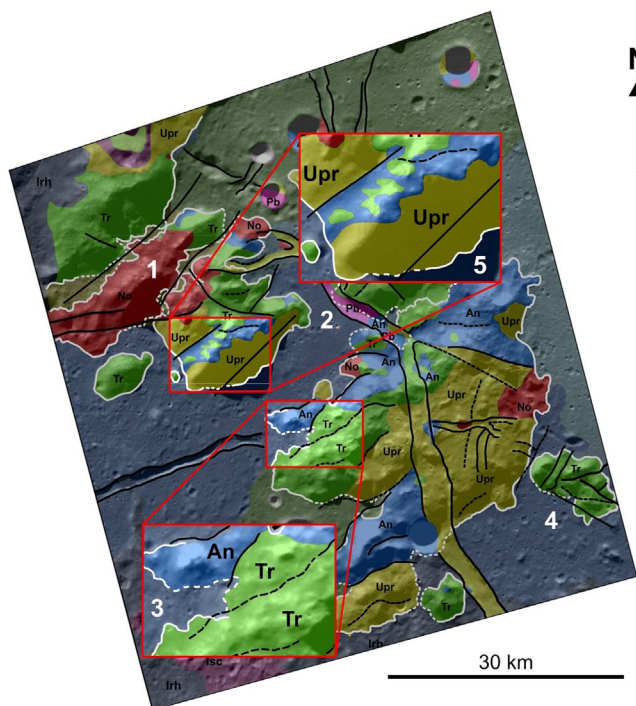


Figure 7. Examples of interpreted magmatic and faulted contacts mapped in the SWPR area. In the bottom-left inset, a faulted contact separates inferred anorthositic (An) and troctolitic (Tr) mineralogies. In the top-right inset, magmatic contacts separate anorthositic (An) and troctolitic (Tr) mineralogies.

We interpret that troctolitic exposures can be found in both magmatic and faulted contacts with other peak-ring mineralogies. Fault-bounded blocks of troctolitic rock can be found in the northernmost regions of the NW area of the SWPR (Figure 7, #1). Faults can also be seen cross-cutting regions of troctolitic rock (Figure 7, #3), which is less common in the other peak-ring mineralogies. We interpret that there are several places throughout the SWPR that show clear evidence of troctolitic outcrops potentially in magmatic contact with anorthositic outcrops. Most notably, small pockets of troctolitic material are completely surrounded by anorthositic material in the southern regions of the NW portion of the peak ring (Figure 7, #4). The emplacement of troctolitic material within

anorthositic material provides the most compelling evidence for magmatic contacts in the entire SWPR area, as the troctolitic material may have crystallized during the same event or may be intrusions into the anorthositic crust.

Anorthositic exposures are also commonly found at the base of mounds in magmatic contact with troctolitic material (Figure 7, #5). This finding could suggest that some smaller mounds (e.g., the southeastern area of the map) may only expose the deeper crustal mineralogies (e.g., troctolitic), whereas shallower crustal mineralogies (e.g., anorthositic and noritic) may have been completely removed and displaced during peak-ring formation.

The distribution of M^3 data in the SWPR could potentially indicate layered sequences of magmatic mineralogies in this region; thus, Kramer et al. (2013) highlight the need for further high-resolution studies in the SWPR. The juxtaposition of peak-ring mineralogies does not solely appear to be due to uplift processes during the Schrödinger basin formation. Magmatic contacts between crustal mineralogies are likely preserved within the SWPR, providing an opportunity to investigate the magmatic history in the mid to lower lunar far-side crust.

3.1.2. Radially Oriented Features

Faults (not associated with the graben) in the SWPR extend radially outward from the center of the basin (Figure A2). This is in stark contrast to the concentric orientation that peak-ring faults typically show, with progressive offsets toward the center of the basin (Dence et al. 1977). This deviation in fault orientation suggests that fault blocks within the peak ring may have undergone rotation during peak-ring formation. One possible cause of the rotation may have been due to interactions among ancient basins during the Schrödinger impact event, such as the Amundsen–Ganswindt, which lies just south of the southwest portion of the Schrödinger basin. The study area with radially oriented faults lies in the thinner crust (~20 km) region of the Schrödinger basin (Kring et al. 2017). However, casual observations of the topography in the thicker crust (~40 km) region of the peak ring to the northeast suggest radial features may also be present elsewhere in the peak ring (Figure 2).

Conversely, the main graben in the SWPR, which trends N–S across the mapping area, has a basin-concentric orientation. The graben also cross-cuts many of the radially oriented faults. The graben orientation suggests that at least this main graben postdated the complex radial faulting and conforms with the expected concentric orientation of faults within peak-ring structures (Kramer et al. 2013; Kring et al. 2016). This type of graben was most likely induced by intrusive igneous activity via the opening of dikes that have lunar mantle depth and composition (Klimczak 2014). Kumar et al. (2016) mapped fallen boulders and boulder trails throughout the Schrödinger basin. They found that grabens (including the one cross-cutting the SWPR study site) host the largest number of boulder fall sites. These boulder falls and associated trails have been interpreted to be a consequence of impact events and recent seismic activity (recent shallow moonquakes; Kumar et al. 2016).

As with interpreting faulted contacts between spectral units, understanding the origin of the radially oriented structural features in the SWPR would require further modeling of the Schrödinger impact event. Future work to investigate the orientation of faults within other regions of the Schrödinger peak-ring material may also provide further insights into basin-forming mechanisms.

4. Traverse Proposals

To better study the lunar far side and south pole, space agencies are collaborating on the Lunar Orbital Platform-Gateway (also known as the Lunar Gateway; Hufenbach et al. 2015; Burns et al. 2019; International Space Exploration Coordination Group 2018). The Lunar Gateway will serve as an outpost for a short-term stay in lunar orbit. It will be used for dispatching and teleoperation robotic missions and will serve as a staging point for crewed missions. The ESA, the Canadian Space Agency (CSA), and the Japanese Aerospace Exploration Agency are collaborating on a robotic transport system, HERACLES (Hiesinger et al. 2019). HERACLES comprises elements that land and operate a rover on the lunar far side, and return rock and regolith samples to the Lunar Gateway for eventual return to Earth. Not only will the HERACLES concept provide opportunities for scientific and economic research at the lunar south pole, but it will also provide technology demonstrations that will pave the way for sustaining human presence on the surface of the Moon via NASA's Artemis program.

Previous studies of potential rover traverses in the Schrödinger basin include the work of Potts et al. (2015), who created 14 day traverses at two sites: one on the east side of the peak ring near the pyroclastic vent, and one on the north side of the peak ring (Figure 2). Additionally, Steenstra et al. (2016) proposed two human-assisted sample return traverses in Schrödinger for the HERACLES mission concept that would explore the pyroclastic vent and the basin wall. Work by Bickel et al. (2019), Sargeant et al. (2020), and Bickel & Kring (2020) have recently shown that terrain types such as pyroclastics and permanently shadowed regions (PSRs) are to be included in the list of trafficable sites for future robotic and crewed missions. Here we explore traverse options in the SWPR area of the Schrödinger basin, a region that has not been examined as a potential landing and traverse site, even though it has

multi-kilometer-long exposures of anorthositic and olivine-bearing peak-ring mineralogies (Kring et al. 2017).

The aims of a traverse in the SWPR area are to sample outcrops and investigate mineralogical contacts. The area is structurally complex, provides insights into peak-ring formation, and enables ground-truthing of satellite observations, including M^3 data. To plan a traverse that would achieve these aims, the rover specifications and the duration of the mission (i.e., one lunar day or multiple years) were considered. Using the finalized SWPR map (Figure 4), we determined a high-priority location for human-assisted robotic rover traverses (after the HERACLES concept: Landgraf et al. 2015).

Selecting the proposed traverse site for a future robotic sample return mission required identifying individual outcrops, mineralogical contacts, and structural features that will address high-priority NRC science goals. Within the SWPR region, our proposed traverse site offers opportunities to collect in situ samples of outcrops and boulders with a known origin. Collecting samples in place from known outcrops yields important contextual information, such as the textures and mineralogical relationships visible in the outcrop where the sample is collected. This additional information potentially allows for a more robust sample to be collected.

5. Features of Interest Methodology

Initial investigations in the SWPR area for a human-assisted robotic traverse focused on locations of features of interest and traverse limitations (e.g., rover speed, mission duration, and terrain). First, the team identified areas of the SWPR with the highest density of potential features of interest. Using the completed geologic map (Figure 4) as a guide, NAC images were rendered to identify and mark all occurrences of boulders and boulder fields, fresh craters, ejecta, secondary craters, regolith, peak-ring material, outcrop exposures (Figure A7), PSRs, and other shadowed areas (with the potential to preserve volatile compounds).

The various methods used to identify the different types of features of interest in the SWPR are detailed below, in addition to using the geologic map of the area. Each feature of interest was recorded on custom-shape layers in JMARS, using color-coded points and polygons. To determine if the SWPR area is a viable region for a traverse, a LOLA slope map (Figures A8, A9) with a resolution of $29.63 \text{ m pixel}^{-1}$ was overlaid onto the mapped region in JMARS.

6. Traverse Limitations

6.1. Duration—One Lunar Day

The selected traverse region (Figure 8) is best suited for a 14 day mission plan, or one lunar day, similar to the 14 day robotic mission presented by Potts et al. (2015). There are accessible mineralogical and structural features in close proximity within the SWPR. This proposal is in contrast to long-term, three-year missions requiring multiple lunar ascent vehicles (LAEs), such as that investigated by Steenstra et al. (2016). To account for unforeseen problems, we included a 30% margin in the traverse schedule which gives a working maximum of 9.8 days per traverse route.

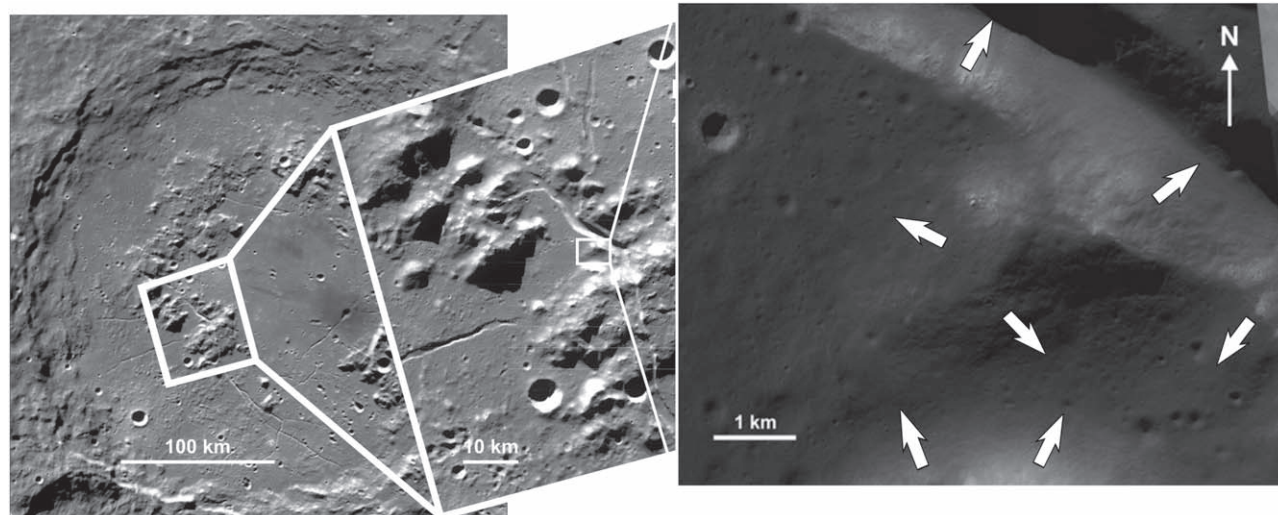


Figure 8. Site for potential 14 day traverse within the SWPR. The traverse region is located between the two massifs and a ~ 4 km graben that cross-cuts the peak-ring structure (left panel). In the northwest area (right panel) is a ~ 600 m diameter relatively fresh crater, exposing the Schrödinger impact melt material. The arrows represent the direction of the downward slope on the massifs and SW graben wall (right panel).

6.2. Solar Irradiance

Because current lunar rover designs use solar-powered batteries, it is important to consider the amount of direct sunlight they would receive during a traverse. We used the Surface Lighting tool from NASA's Moon Trek (<https://trek.nasa.gov>) to compile solar irradiance data in the proposed traverse site. The optimal periods had 13 days of illumination and were at the start of early 2022 (day 001–day 013), 2023 (day 020–day 032), and nearing the end of 2024 (day 334–day 346), and 2025 (day 352–day 346).

6.3. Rover Speed and Distance Traveled

In order to accurately plan a traverse, one of the most important specifications is the rover speed, as this limits the distance the rover can travel in a given time period. Two rover speeds have been proposed for the Potts et al. (2015) and Steenstra et al. (2016) missions, with the speeds based on the designs of other lunar platforms. Potts et al. (2015) assumed a rover speed of 1.7 km hr^{-1} based on Lunokhod 1 and 2 performance, and the lunar-roving vehicles used in Apollo 15, 16, and 17. Alternatively, Steenstra et al. (2016) assumed a reduced rover speed of 0.36 km hr^{-1} , based on the estimated speed of the Resource Prospector rover (Loftin et al. 2013). The reduced rover speed was constrained by the estimated maximum time needed for communications relay through the Lunar Gateway, as outlined in the International Communication System Interoperability Standards (IASIS 2018) and the operational speed required for a neutron spectrometer (Loftin et al. 2013). For the SWPR traverse, we implement the 0.36 km hr^{-1} speed used by Steenstra et al. (2016). The rover traverse must begin and end at the landing site, as this mission assumes no additional LAEs at different sites. Therefore, the traverse distance was restricted to a range where it can safely return to the LAE at the landing site.

6.4. Slope

Previous work showed that wheel-based rovers can experience difficulties due to a loss in wheel traction and excessive wheel sinkage associated with inclined terrain near craters and

at the base of certain slopes (Costes et al. 1972; Carrier et al. 1991; Seeni et al. 2010; Potts et al. 2015; Steenstra et al. 2016; Bickel & Kring 2020). Therefore, using the $29.63 \text{ m pixel}^{-1}$ LOLA slope map the proposed traverse routes and features of interest are restricted to $<15^\circ$ to ensure rover trafficability (Potts et al. 2015; Steenstra et al. 2016), and all features of interest are located on accessible slopes. However, the slope limitation prevents accessible sampling of outcrops close to structural features and outcrops on steep slopes. In these cases, boulder tracks and boulders were selected as target sites when the safe slope limitation was exceeded; displaced boulders allow for the sampling of otherwise inaccessible mineralogies.

7. Potential Traverse Paths

The proposed landing site is a 200 m ellipse located in a relatively flat (0° – 2°) area (equivalent to Apollo 12; p. 610, Heiken et al. 1991). The landing site was chosen because there are diverse rock outcrop exposures as well as structurally interesting features in the traverse vicinity (Figure 9). The traverse region is located between two massifs adjacent to the graben (Figure 8). There are four sites of interest near the landing ellipse that contain boulders and regolith for sampling. One site is near the base of a massif and contains noritic, troctolitic, and anorthositic mineralogies. Another site contains troctolitic, anorthositic, and pyroxene-bearing anorthositic mineralogies. The third site is at the upper rim of the graben, where there is a pyroxene-bearing anorthositic boulder. The last site is a boulder field of noritic impact ejecta. These sample sites were chosen because they are located on traversable slopes ($<15^\circ$) and have scientific significance for addressing important goals from the NRC (2007) report. We designed three separate traverses (A, B, and C), presented in Figure 9. Each traverse allows access to different features of interest and answers different goals from the NRC (2007).

7.1. Ideal Traverse

An ideal traverse, omitting time and instrument payload constraints, visits each of the mineralogical and geomorphological features of interest within the SWPR area. These

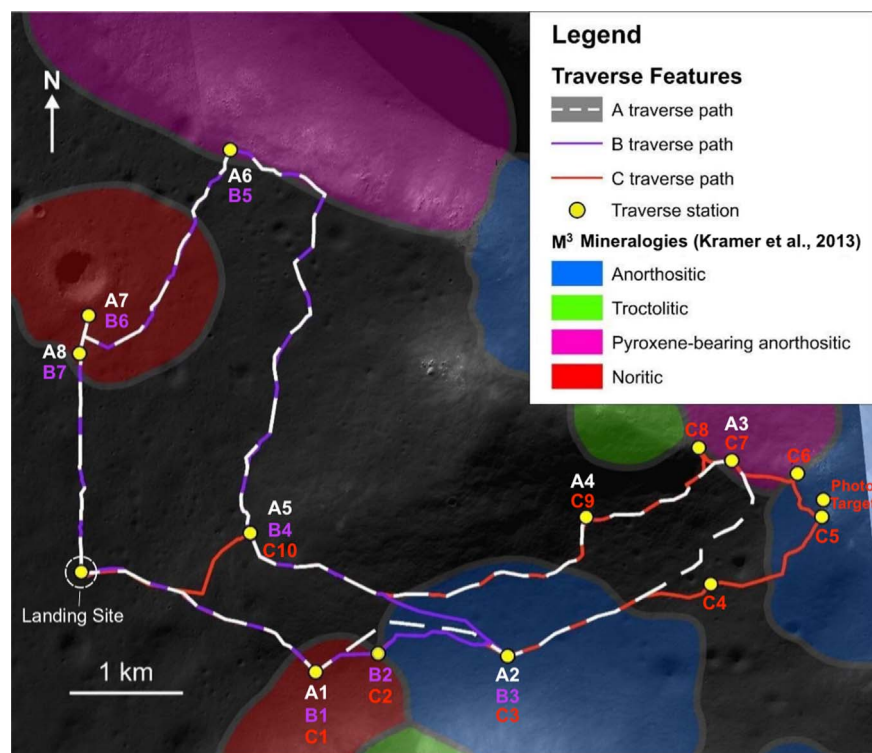


Figure 9. Potential traverse paths in the SWPR area. Traverses A, B, and C contain stations at each spectral unit identified by M^3 data, as well as boulder samples and imaging stations along the graben. Traverses A and B provide the opportunity to sample two impact breccia boulder samples at the small impact crater, whereas Traverse C allots time for sampling at contacts between spectral units.

outcrops include noritic, anorthositic, pyroxene-bearing anorthositic, and troctolitic material. The geomorphological sites of interest include the graben in the northern extent of the region (Station A6/B5) and a relatively fresh crater located north of the landing site (Stations A7/B6, A8/B7). Another site of interest includes a frequently shadowed region south of some peak-ring material where there may be an opportunity to sample buried volatiles northwest of the landing site (NRC 2007 goals 4a, 4b, 4c). Additionally, there is a low-albedo feature south of the landing site adjacent to an anorthositic outcrop, which may be a pyroclastic deposit or a unique mineralogical contact. If this feature is a pyroclastic deposit, the traverse offers the additional opportunity to address NRC (2007) goals 5c and 5d, pertaining to lunar volcanism. If the feature has an exposed contact with the anorthositic outcrop as a mineralogical contact, it would help address science concepts related to the stratigraphy of the lunar crust and the lunar magma ocean hypothesis (NRC (2007) goals 1c, 2a, 2b, 2d, 3a through 3d). These extra sites of interest are included here to highlight the additional sites that could be reached given potential technological advances in rover speed and slope mobility.

7.2. Features of Interest along Proposed Traverses

In order to identify boulders associated with mineralogical outcrops, we first considered those in proximity to outcrops identified during the geologic mapping process using the method described above. Once accessible boulders were identified, M^3 mosaics and data from Kring et al. (2016) were reviewed to determine if mapped outcrops were overlying the data. We preferentially reviewed outcrops that are directly associated with M^3 data over outcrops where mineralogies are

only inferred. To verify the source outcrop of selected boulders, we traced boulder tracks upslope to the portion of the outcrop where the boulder originated, where possible.

Reflectance spectra from the M^3 instrument suggest the boulders surrounding the crater have a noritic signature (Figure 9, stations A7/B6 and A8/B7). Additionally, the literature interprets the bulk composition of the impact melt sheet in Schrödinger as being noritic (Kramer et al. 2013).

Young, well-preserved craters can aid in determining the age of the lunar surface and in better understanding the cratering process of the inner solar system. The crater appears to be young (relatively fresh), because of the less deformed crater rim compared to surrounding craters and the abundance of ejecta around the crater rim (increased boulders and high-albedo rays), which could be sampled to determine its age. The crater would have an exposed impact melt sheet and breccia associated with it, which could also be sampled.

The NW–SE trending graben is an accessible photography target during two of our proposed traverses (Figure 9, stations A6/B5). The graben was identified and mapped using techniques described in Appendix A.2. The graben and radial fault orientation demonstrate the complexity of peak-ring formation in impact basins. As mentioned previously, faults are typically oriented concentrically in impact structures, aligning with larger geologic features such as grabens, floor-fractured features, and the mountainous peak-ring terrain. Floor-fractured features are associated with volcanic activity beneath the impact basin (Schultz 1976; Jozwiak et al. 2015). The presence of floor fractures and no volcanic or pyroclastic flows implies magma accumulated beneath the basin but never penetrated through the surface (Jozwiak et al. 2015). Obtaining high-resolution images of the graben walls and mapped fault lines cross-cutting peak-ring mineralogies at the SWPR

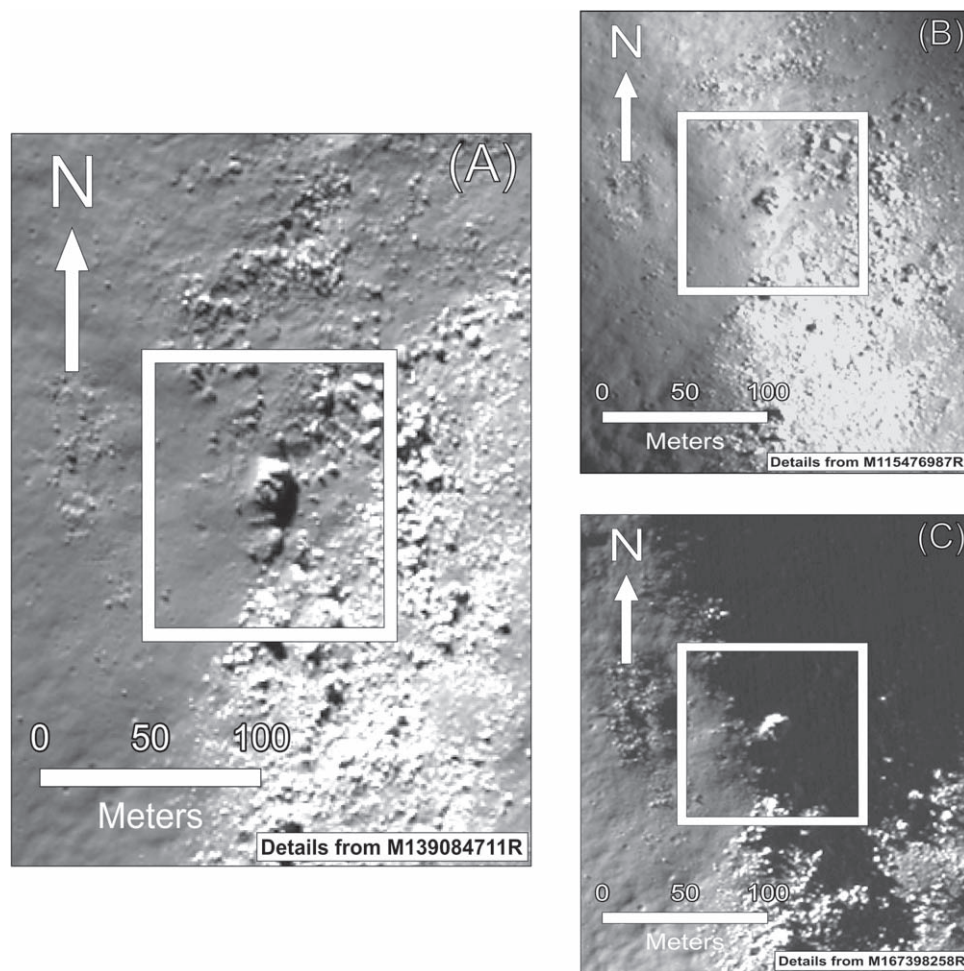


Figure 10. (A) Image of the banded boulder along traverse route C. (B) and (C) show different lighting conditions of the boulder, in which the bands are still present. M^2 spectral data of the boulder suggest an anorthositic mineralogy. The sample lies in a slope region above 15° and so cannot be sampled; however, the site is recommended as a photography target during the traverse (NAC Image IDs: M139084711R, M115476987R, M167398258R).

traverse paths would provide new context for the unusual structural processes involved in impact basin formation. Samples from the graben wall and peak-ring mineralogies at fault contacts would provide chronological information on the uplift timing and displacement of the lunar crustal material. With the traverse paths being located directly on a mapped fault line, the chances of acquiring images and samples (e.g., mylonites or pseudotachylites) related to the fault is high. The orientation of the fault would also grant the opportunity to investigate the proposed magmatic contacts with the noritic, anorthositic, and troctolitic mineralogies.

We identified a banded boulder that would be in range for high-resolution imagery (Figure 10). This boulder appears to have horizontal, dark-light striping in NAC images with different illumination conditions; i.e., it is not an artifact of shadowing. High-resolution photography of the banded boulder may reveal the nature of any cryptolayering, which can be compared with other banded boulders that have been identified on the Moon to better understand their magmatic origin (Kickapoo Lunar Research Team & Kramer 2014).

7.3. Proposed Traverses

Considering constraints on traverse duration, feasible slope mobility, and rover speed, we present Traverses A, B, and C, which are possible to complete within a 14 day timeline

(Table 1). Each of the three traverses begins and ends at the landing site ($75^\circ 54'S$ $126^\circ 72' E$), where the LAE would be stationed to return samples to the Lunar Gateway. Landing within this area of the Schrödinger basin enables immediate sampling of the impact melt sheet, allowing returned samples to provide an absolute date on the Schrödinger impact event. If the sample collected includes impact melt from the SPA basin, it may be possible to determine the timing of the SPA basin-forming impact. Site information for the traverses is summarized in Table 1, and detailed stop information for each traverse can be found in Appendix B (Tables A1–A3).

7.3.1. Traverse A

Traverse A (Figure 9, dashed path) contains the highlights of both B and C, in an attempt to maximize the diversity of samples and science goals addressed in the NRC (2007) report. The traverse is 25.0 km long, covering the greatest distance of the three proposed routes. Traverse A is designed to sample each of the four major inferred mineralogies: noritic, anorthositic, pyroxene-bearing anorthositic, and troctolitic rocks, as well as to offer an opportunity for high-resolution imagery of structures within the graben walls.

Site A1 ($-75^\circ 58'S$, $127^\circ 01' E$) samples a noritic boulder. Site A2 ($-75^\circ 56'S$, $127^\circ 54' E$) samples an anorthositic boulder east of Site A1. The traverse then extends north, toward the graben

Table 1
Station Information for Each of the Three Proposed Traverses

| Station ID (A) | Station ID (B) | Station ID (C) | Latitude | Longitude | Elevation (m) | Slope (deg) | Surface Unit ^a | M ³ Interpretation | Sample Type and Minimum Mass (kg) |
|----------------|----------------|----------------|----------|-----------|---------------|-------------|---------------------------|---------------------------------------|-----------------------------------|
| LS | LS | LS | -75.54 | 126.72 | -8066 | 0.48 | Ish | n/a | Regolith/Rake: 2.0 |
| A1 | B1 | C1 | -75.58 | 127.01 | -7969 | 13.67 | pNpr | Noritic | Crystalline Boulder: 0.5 |
| ... | B2 | C2 | -75.57 | 127.1 | -7925 | 10.72 | pNpr | Anorthositic/ Noritic | Regolith/Rake: 2.0 |
| A2 | B3 | C3 | -75.56 | 127.54 | -7859 | 14.35 | pNpr | Anorthositic | Crystalline Boulder: 0.5 |
| ... | ... | C4 | -75.56 | 127.54 | -7818 | 2.25 | pNpr | n/a | Regolith/Rake: 2.0 |
| ... | ... | C5 | -75.54 | 127.69 | -7772 | 6.9 | pNpr | Anorthositic | Crystalline Boulder: 0.5 |
| ... | ... | C6 | -75.52 | 127.66 | -7913 | 9.64 | pNpr | Anorthositic/Pyx-bearing Anorthositic | Regolith/Rake: 2.0 |
| A3 | ... | C7 | -75.52 | 127.58 | -7731 | 7.18 | pNpr | Pyx-bearing Anorthositic | Crystalline Boulder: 0.5 |
| ... | ... | C8 | -75.51 | 127.54 | -7707 | 7.09 | pNpr | Pyx-bearing Anorthositic/Troctolitic | Regolith/Rake: 2.0 |
| A4 | ... | C9 | -75.53 | 127.38 | -7660 | 9.1 | pNpr | n/a (Troctolitic) | Crystalline Boulder: 0.5 |
| A5 | B4 | C10 | -75.53 | 126.94 | -7918 | 6.93 | pNpr | n/a | Regolith/Rake: 2.0 |
| A6 | B5 | ... | -75.4 | 126.96 | -8068 | 0.6 | Ish | Pyx-bearing Anorthositic | Crystalline Boulder: 0.5 |
| A7 | B6 | ... | -75.45 | 126.76 | -8058 | 2.15 | Ish | Noritic | Brecciated Boulder: 5.0 |
| A8 | B7 | ... | -75.47 | 126.74 | -8075 | 0.93 | Ish | Noritic | Brecciated Boulder: 5.0 |

Note.

^a Kramer et al. (2013).

where a pyroxene-bearing anorthositic boulder is sampled at Site A3 ($-75^{\circ}52\text{S}$, $127^{\circ}58\text{E}$). Site A4 ($-75^{\circ}53\text{S}$, $127^{\circ}38\text{E}$) is at a boulder downslope of an outcrop of troctolitic material. Although the outcrop itself lies at the crest of a hill with slopes too steep for a rover to safely traverse, boulder tracks were traced down the slope from outcrop to boulder, leading us to conclude that this boulder originates from the outcrop. The rover then traverses westward around the base of the hill, taking a regolith/rake scoop at Site A5 ($-75^{\circ}53\text{S}$, $126^{\circ}94\text{E}$). The traverse leads north to the edge of the graben. Traveling west along the ridge provides opportunities for photographing structural features across the graben before sampling another pyroxene-bearing anorthositic boulder at Site A6 ($-75^{\circ}40\text{S}$, $126^{\circ}96\text{E}$). The traverse then leads south, toward the landing site. The traverse stops at the relatively fresh crater to sample ejecta at two distances from the crater rim at Sites A7 and A8 ($-75^{\circ}45\text{S}$, $126^{\circ}96\text{E}$; $-75^{\circ}47\text{S}$, $126^{\circ}74\text{E}$) before returning to the landing site.

In summary, Traverse A samples each mineralogy in the SWPR. It also provides an opportunity to sample the Schrödinger impact melt sheet material at the fresh crater and image structural features at the graben at both the northeast and northwest sites. The total sample mass from traverse A is 16.5 kg (Table 1). Sites A1–A5 are located at the base of a slope, where it is possible that soft regolith may have accumulated (Carrier et al. 1991). The majority of sites in Traverse A are located on slopes $<10^{\circ}$, with the exception of Sites A1, A2, and A4. In addition, the route from site A3 to A4 requires the rover to traverse laterally along a slope.

7.3.2. Traverse B

Traverse B (Figure 9, purple path) is 18.6 km long and does not extend to the northeast segment of the graben. It is the only traverse plan to implement in situ analysis at each station, as well as sample acquisition, requiring a larger instrument suite than Traverse A or C (Appendix, Table A4). After sampling anorthositic material, the route circles back and travels north to the northwest graben exposure, collects a sample of pyroxene-bearing anorthositic material, and then samples crater ejecta, like Traverse A.

Traverse B starts eastward, collecting noritic and anorthositic boulder samples (A1 = B1, A2 = B3; See Table 1). However, unlike Traverse A, Traverse B is designed to stop and collect a regolith/rake sample at the inferred contact between noritic and anorthositic mineralogies (Site B2, $-75^{\circ}57\text{S}$, $127^{\circ}10\text{E}$). After collecting the anorthositic sample at Site A2/B3, Traverse B backtracks, heads west, and collects a regolith/rake sample at the same location as A5. Traverse B then follows the same path as Traverse A for Sites B4–B7 until its return to the landing site. Sites B1–B3 are located at the base of a hill where the slope is $>10^{\circ}$. Travel between these three sites would require traversing laterally along the base of the slope.

Traverse B focuses more on geomorphological features than Traverses A or C. Traverse B samples both the edge of the graben (northwestern site) and material from a nearby fresh crater ($\sim 600\text{ m}$ diameter, $\sim 20\text{ m}$ depth). Like the other two traverses, Traverse B samples the noritic, anorthositic, and pyroxene-bearing anorthositic mineralogies. Similar to Traverse A, an advantage of Traverse B is that it may present an opportunity to sample Schrödinger impact melt material. The total sample mass from Traverse B is 17.5 kg (Table 1).

7.3.3. Traverse C

Traverse C (Figure 9, red path) is the shortest of the three, at 17.2 km long. It does not visit the small crater or northwest section of the graben. Instead, it focuses on collecting all four mineralogies and contacts between units.

Stations C1–C3 are the same as Sites B1–B3 (Table 1). After sampling the anorthositic boulder, Traverse C is directed northward, much like Traverse A, but with additional sites of interest. Site C4 ($-75^{\circ}56\text{S}$, $127^{\circ}54\text{E}$) is designed to collect a regolith/rake sample between two anorthositic signatures observed in the M^3 data, both as a means to ground-truth M^3 data and to better understand the physical properties of lunar regolith and talus. Traveling up the hill toward the graben, Site C5 ($-75^{\circ}53\text{S}$, $127^{\circ}69\text{E}$) is selected for another sample of anorthositic material at an outcrop exposed by the graben. Site C5 provides a closer sample of potentially similar mineralogy to the banded boulder and is also on a more accessible slope than the unreachable banded boulder. Smaller boulders at Site C5 will also be investigated for layering similar to the banded boulder. Between Sites C5 and C6 is a potentially banded boulder on a steep slope that is a prime photography target. Site C6 ($-75^{\circ}52\text{S}$, $127^{\circ}66\text{E}$) is located where the M^3 data transition from anorthositic to pyroxene-bearing anorthositic signatures. This potential contact is suggested to be a rake sample, with the opportunity to image any clear contact details. Site C7 is equivalent to Site A3, sampling the same pyroxene-bearing anorthositic boulder. Traverse C then travels along the graben westward, collecting both a boulder and rake sample at Site C8 ($-75^{\circ}51\text{S}$, $127^{\circ}54\text{E}$), where there may be contact between pyroxene-bearing anorthositic and troctolitic material. Returning downslope to the southwest, Site C9 is equivalent to Site A4 with the intention of sampling troctolitic material. En route to the landing site, Site C10 is equivalent to both A5 and B4. Sites in Traverse C share the same issues for rover trafficability as those described in Traverses A and B.

Traverse C focuses on both ground-truthing the M^3 data interpretations, as well as understanding the relationships between mineralogies. It samples the noritic, anorthositic, and pyroxene-bearing anorthositic materials, as well as the potential to sample troctolitic material downslope of an outcrop. Traverse C emphasizes visiting mineralogical contacts to better understand magmatic relationships. One feature of interest in Traverse C that is not encompassed in either A or B is the opportunity to photograph a boulder that appears to be banded (Figure 10). The opportunity to measure such banding would enable studies of the complex igneous processes that occurred in the lunar subsurface (Kickapoo Lunar Research Team & Kramer 2014). In contrast, Traverse C is unlikely to sample any fresh impact melt material, and there is no exposed Schrödinger melt sheet material along its path. The total sample mass from Traverse C is 16.5 kg (Table 1).

7.4. Summary of Traverses

Traverses A, B, and C sample multiple peak-ring mineralogies (noritic, anorthositic, pyroxene-anorthositic, and troctolitic materials) excavated from depths of 15–26 km in the lunar crust (Kring et al. 2016). Most notably, the traverses proposed here provide a spectacular new opportunity to collect samples from known outcrops on the lunar surface—a sharp contrast to Apollo samples of which none originated from outcrops. Unfortunately, within the landing region, the best

exposure of troctolitic rock (thought to have been exhumed from the deepest parts of the lunar crust) is exposed at a higher elevation on peak-ring mounds. Therefore, it is not possible for a rover to safely traverse the slopes leading up to a troctolitic outcrop, but this mineralogy can still be sampled from boulders found downslope of the exposure. The traverse path also provides an opportunity for imaging the troctolitic outcrop from the base of the slope. High-resolution imagery can be used to observe outcrop scale structural features that can facilitate additional deductions about the outcrop origins. Each traverse has unique advantages and is optimized to address different science objectives regarding geomorphological features and target potential contacts between spectral units. Traverse A was planned to maximize the diversity of scientific outcomes by traveling through each spectral unit and structural feature to obtain a broad overview of the SWPR. In contrast, Traverse B is the only traverse that includes in situ analysis at each station, providing abundant data even before sample return. Traverse B also includes sampling and imaging structural features, like the crater ejecta and the graben. Traverse C focuses on magmatic crustal evolution by sampling each type of mineralogy, and all potential contacts among them, but does not visit the crater. If the total sample mass on any traverse remains below the sample container mass limit, then at most two samples could potentially be collected from certain stations. Crystalline boulder samples would be prioritized for a second sample, because these rock samples have the potential to address more NRC science goals (e.g., 1a, 1b, 1c, 2a, 2b, 2c, 3a and 3b) than regolith samples. While fragments suitable for sampling may exist near large boulders, a technique for subsampling them may be needed.

8. Conclusions

A detailed map of the SWPR reveals interesting radial fault orientations extending from the basin center that agree with the findings from previous studies in this area by Kramer et al. (2013) and Kring et al. (2016). These types of observations open the doors for further Schrödinger basin impact modeling, particularly concerning the effects of preexisting impact basin structures (Shoemaker et al. 1994). The faulted and magmatic contacts observed between the peak-ring mineralogies further highlight the potential for the SWPR area to address many high-priority NRC (2007) goals by providing an opportunity to investigate the magmatic history of the far-side crust. Further, there is still abundant peak-ring material, crater floor, and walls that can be mapped at a similar resolution to the maps presented here.

The geologic map was used to design notional robotic traverses that address science priorities (NRC 2007). We provided three traverse options within the SWPR that are each achievable within a 14 day mission timeframe for robotic missions. Although a rover on the lunar far side can be controlled from Earth, valuable time would be lost due to communication delays. Telerobotic communications can be optimized if the rover is controlled in near-real time by a human operator from the Gateway. The detailed traverse plans highlight an abundance of interesting features in the SWPR area, such as the heterogeneous boulder that would be an exceptional target for future sample return missions. Additionally, the ability to take photographs and samples near a large graben provides context for post-impact tectonism and how subsequent magmatism and volcanism continued to shape the

surface of the Moon. Studying the graben may provide answers to the timing of uplift and displacement of lunar crustal material. As the Lunar Gateway project is further developed and the next lunar rover missions constrained, these traverses can be considered for their scientific potential, should they meet the upcoming demands of the lunar science community.

The Schrödinger basin remains an enigmatic target for lunar exploration. Its unique status as a young crater on the lunar far side within the SPA Basin lends to it being a prime target for a human-assisted robotic mission.

The authors would like to acknowledge the support of the Lunar and Planetary Institute (LPI) in Houston, TX, and the Universities Space Research Association. The research was performed as part of the Exploration Science Summer Intern Program hosted by the LPI and the NASA Johnson Space Center in Houston, TX, which was supported by NASA Solar System Exploration Research Virtual Institute contracts NNA14AB07A and 80NSSC20M0016. The authors would like to acknowledge the JPL Moon Trek team for assistance with NAC imagery throughout the Schrödinger basin and Katharine Robinson of the LPI for insight on geologic mapping and support with the overall research. This is LPI contribution No. 2582.

Appendix A Additional Maps

Before rendering the final geological map of the SWPR region (Figure 4, main text), the team extensively mapped craters, impact ejecta, outcrops, faults, grabens, talus, and low-albedo features. This section provides a detailed explanation as to how these features were mapped and provides specialized geological maps of the SWPR that highlight each feature type.

A.1. Craters, Ejecta, and Talus

Craters are circular depressions with raised rims on the basin floor which may or may not be surrounded by a blanket of rocky material (ejecta). Craters and ejecta were mapped independently as two separate custom polygon shapefiles in JMARS using LROC NAC images. The largest craters (diameter >1 km) in the region were mapped first, followed by relatively fresh, smaller craters. The relative preservation state of each fresh crater was determined by the roundness of the crater rim and the abundance of ejecta/roughness. Fresh craters are generally rounder, have less deformed rims with high-albedo ejecta rays, and have boulders located along the crater rim (Campbell 2012; Carter et al. 2012). When a crater was identified, we used LOLA topographic data and WAC mosaics to ensure that the features were concave and not convex domes mistaken due to lighting angles. The perimeters of the craters were outlined along the approximate high points of the crater rim. If crater rims were difficult to determine, lines were drawn toward the inner face of the crater rim so as not to overestimate the crater diameter. In craters with large shadows, this estimation often led to crater outlines along the outer edge of the shadow. Ejecta was mapped as higher-albedo rays that border some craters. This included boulders that appeared to be sourced from the cratered area. When available, Clementine FeO maps in JMARS and the Diviner Nighttime Soil image in QuickMap were also used to differentiate ejecta from regolith. We used circular polarization ratios from hybrid polarimetry

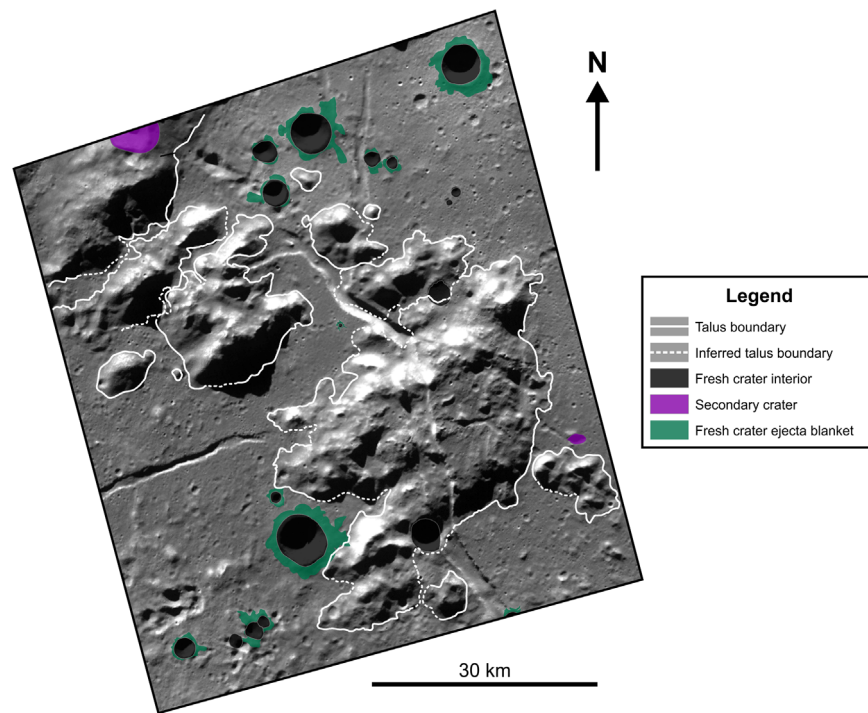


Figure A1. Mapped craters, well-preserved ejecta blankets, secondary craters, and talus material in the SWPR area. Only craters >1 km were mapped. The solid lines outline known talus extent boundaries, dashed lines indicate inferred boundaries.

Mini-RF radar data sets in QuickMap to identify ejecta that were not observable using Diviner Nighttime Soil and Clementine FeO data sets, or high spatial resolution ($0.5\text{--}1$ m pixel^{-1}) NAC images. Ejecta blankets exhibit decimeter-scale roughness that is detectable using S-band (12.6 cm wavelength) data from the Mini-RF instrument (Campbell 2012; Carter et al. 2012; Neish et al. 2017).

Talus is material from the peak ring that has accumulated at the base of slopes as a dry-flow deposit, comprising fragments of the peak-ring mineralogies and entrained regolith. Talus was initially identified using NAC images with solar incidence angles of $60^{\circ}\text{--}90^{\circ}$ and a spatial resolution of $0.5\text{--}1.5$ m pixel^{-1} . The talus boundary is marked by a solid line. Because talus boundaries are often correlated with a break in the slope at the base of a hill or cliff, the talus extent was determined using NAC images at the base of peak-ring material, and the slope break was identified using LOLA slope data. Talus criteria include a lack of craters, relatively smooth appearance, lighter color, boulders, and boulder tracks. Inferred talus boundaries are denoted with a dashed line. These included situations where the boundary of the talus was diffuse, the boundary was intersected by a crater, or the boundary was not illuminated in any of the available NAC images. Talus material covers the base of the peak-ring structure where it is in contact with the smooth and rough hummocky floor material, and in low topographic terrain. Kring et al. (2016) previously mapped talus material over the entire peak-ring structure, which is consistent with the map generated here.

Figure A1 shows a map of craters and talus material within the SWPR. Only craters with diameters >1 km were mapped, because they revealed pyroxene-anorthositic and/or noritic outcrops in their crater walls (from M^3 spectral signatures) and showed relatively well-preserved impact ejecta blankets. The

ejecta blankets and material extend ≤ 1 crater radii from the crater rim.

A.2. Structural Features

In JMARS, NAC images were used to identify structural features, which were subsequently traced using the line tool in a custom-shape layer. Solid lines denote features where the boundary could be traced with certainty. Dashed lines denote features where the boundary was inferred. Kramer et al. (2013) and Kring et al. (2016) mapped structural features in and around the peak ring. Their methods and data set recommendations were applied to our study. Grabens were identified as areas of lower topography bound by two parallel normal faults, creating a linear depressional feature (Figure A2). Lines drawn in JMARS denote the extent of both of the faults bounding the graben. Where the graben was intersected by cratering, the path of the graben was not inferred across the extent of the crater. In some areas, the graben was obscured from view by a shadow in all of the available NAC images. In this situation, LOLA topography was overlaid on a South Pole WAC mosaic to trace the path of the graben using changes in slope and elevation. Faults were identified as linear features marking an abrupt change in topographic height (Figure A2). Where faults could not accurately be traced, they were denoted with a dashed line, as was done for the grabens. No rilles were identified.

Faults, grabens, and linear features cross-cut the peak-ring material, uplifting and exposing impact melt sheet and crustal material (Figure A2). The graben is positioned along a NNW–SSE orientation ($\sim 350^{\circ}$ to 340°), cutting through the entire peak-ring structure in this region. Outcrops of the five mineralogies have been exposed along the walls of the graben and numerous boulder tracks are present on the slopes. Faults are generally oriented radially from the center of the basin,

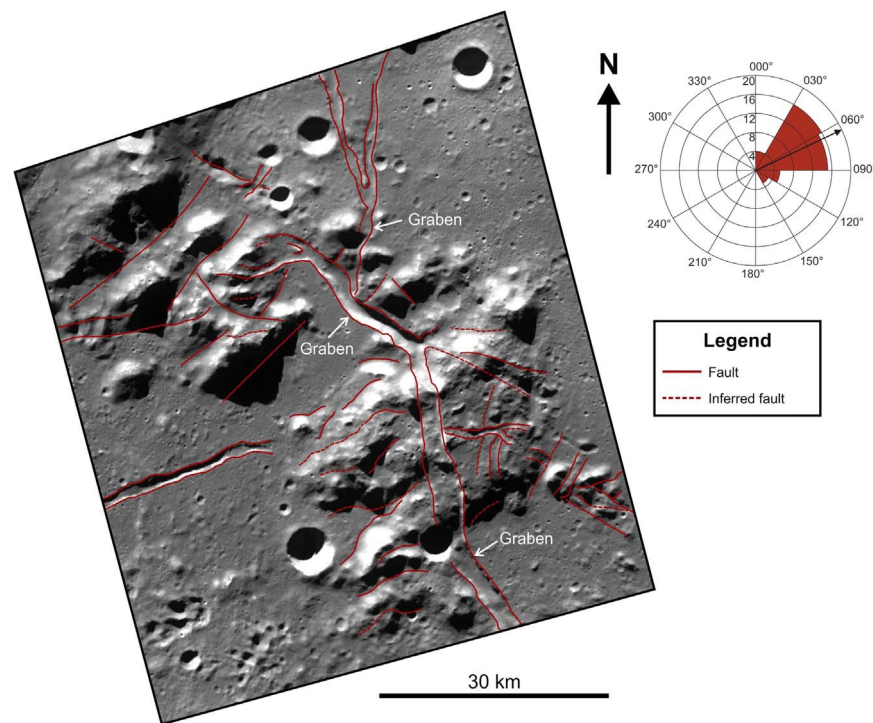


Figure A2. Mapped structural features in the SWPR area. Solid lines mark known fault lines and dashed lines mark inferred fault lines. NAC images were used to outline faults and grabens, and LOLA data were used supplementarily to determine their full extent. The average orientation of faults (excluding grabens) in the SWPR is 064° . These faults are radially oriented with respect to the center of the basin, which lies $\sim 060^\circ$ – 065° from the SWPR.

which is discussed in detail in Section 3.1.2. Floor fractures were initially considered to be either rilles or unidentified linear features. However, further investigation using NAC imagery showed little evidence to suggest the floor fractures are rilles (lack of volcanic material), and instead suggests they are faults. Because the floor fractures connect to faults and the graben, they were mapped as faults, and do not appear to have formed from a separate, brittle deformation process. These floor fractures were therefore mapped as faults.

A.3. Outcrops

Outcrops were initially identified using NAC images with solar incidence angles between 60° and 80° and spatial resolutions of 0.5 – 1.5 m pixel $^{-1}$. Each outcrop was marked as a polygon in a custom-shape layer in JMARS. Crater walls, graben walls, faults, and peak-ring structures were the main targets for possible outcrop exposures, as outcrops are associated with these features on Earth. High-albedo areas and boulder fields were also investigated to search for possible rock exposures. In high-albedo areas, outcrops were inferred if they were located in an area with a gradual slope change. Sharp changes in slope angle would suggest that the high-albedo area was caused by a slope effect rather than an outcrop. We cautiously identified outcrops on sloped or high-albedo, low topographic terrain, because boulders and boulder fields can also produce a high-albedo signature in these examples. Multiple NAC images covering the same area were needed to ensure that exposed outcrops were indeed present. Although NAC images with a high incidence angle typically provide the best illumination for exposing rock faces, in some cases, NAC images with lower incidence angles ($<60^\circ$) were used, because shadows were capable of revealing rock exposures hidden by high-albedo effects. The 3D view in Moon Trek was also

utilized for mapping outcrops, as it provided a way to gain a different perspective of target areas.

The peak-ring structure has numerous outcrops exposed on slopes, especially in the northern section of the SWPR area (Figure A3). If a mapped outcrop was located within an area of M^3 data, the color of the outcrop was changed to match the color of the M^3 data. Outcrops that were not associated with M^3 data could not be reliably identified and were labeled as unknown until future orbiter missions collect additional spectral data.

Outcrops in the SWPR represent crustal, and possibly upper mantle, material from various depths that were excavated, rotated, and faulted during impact basin formation. The excavation depth of the crustal material in the Schrödinger basin was estimated to be 15–26 km (Kring et al. 2016). Using spectral reflectance data from the M^3 instrument, we mapped what are interpreted to be anorthositic ($>90\%$ plagioclase, $<10\%$ pyroxene), pyroxene-anorthositic ($\sim 90\%$ plagioclase, 3%–10% pyroxene), noritic ($<90\%$ plagioclase, $>10\%$ pyroxene), and troctolitic (plagioclase + olivine) outcrops (Kring et al. 2016). Because M^3 data have a coarse resolution of 280 m pixel $^{-1}$, any of the mapped outcrops in the peak ring must expose a significant amount of interpreted minerals to produce differentiable spectral signatures.

Troctolitic and anorthositic outcrops are located throughout the entire mapping area, primarily in the northern and central regions. Noritic outcrops are located in the northern region, with few isolated patches scattered in the central region of the map. Pyroxene-anorthositic outcrops are only found along graben and crater walls, and do not appear to be associated with the peak-ring structures. The southern and southeastern region of the peak-ring structure is lacking in outcrops due to its low topography, and talus and regolith cover. Noritic signatures are

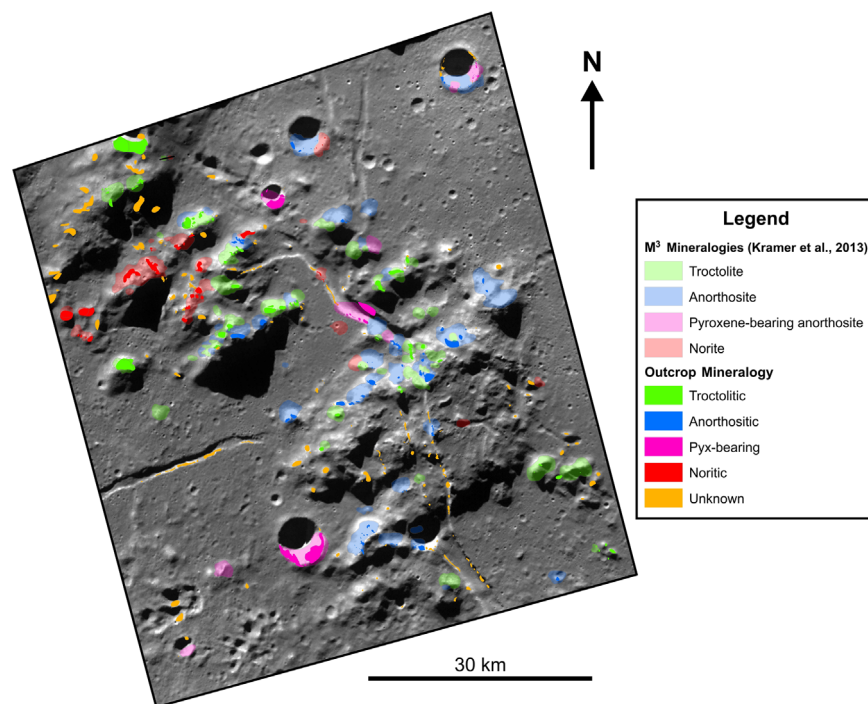


Figure A3. Mapped outcrops in the SWPR area. The outcrops were assigned mineralogies based on their M^3 data signature (Kramer et al. 2013), relative topographic position, and albedo.

isolated in this region of the map; however, LRO NAC images did not reveal any outcrops.

Outcrops that were identified as unknown due to a lack of M^3 coverage were investigated further to determine if their mineralogy could be inferred from topographic and stratigraphic relationships. If an unknown outcrop was located close to an M^3 signature, we initially used NAC images to determine if the unknown outcrops had a similar albedo to outcrops within with M^3 signatures. We then referenced the LOLA DEM slope maps to ensure that no change in topography existed between the unknown and known outcrops. This measure was put in place to avoid making inferences across potential faults within the peak ring. If the unknown outcrop conformed with our criteria, the outcrops were designated a mineralogy (i.e., troctolitic, anorthositic, pyroxene-bearing anorthositic, or noritic). Each unknown outcrop was investigated, and if the criteria above were not met, the unknown outcrop was redesignated as an investigated unknown.

The map in Figure A4 shows all of the outcrops identified based on M^3 spectral signatures, as well as the inferred outcrops and investigated unknowns. In areas with a high density of M^3 data coverage, such as the central and northern regions of the mapped area, the mineralogy of the majority of unknown outcrops could be inferred. Where M^3 data were sparse, more outcrops were designated as investigated unknowns. This was most apparent in areas of the southernmost massif and outcrops located in the walls of the graben.

All of the features mapped in this project were combined to produce the map shown in Figure A5. This combined map illustrates the structural geology, surface features, occurrence of outcrops, and their assigned mineralogy within the SWPR mapping area. This map was created to highlight only the

features mapped as part of this project, although M^3 data from Kramer et al. (2013) were included for reference.

The extent of each mineralogy was mapped using the location of M^3 signatures, changes in albedo, and changes in topography (Figure A6). Where the extent or type of mineralogy could not be determined, these areas remained as a separate mineralogy named “investigated unknown.” Shadowed areas of the peak ring were also designated as investigated unknown, if no illuminated NAC images could be found.

Talus was included in the maps, as it defines the boundary between the peak-ring materials and the basin floor. Faults were also added because they show the nature of some of the mineralogical contacts. The occurrence of each crustal mineralogy varies across the SWPR. Troctolitic and anorthositic mineralogies are exposed as outcrops at various locations across the entire mapping area. Noritic mineralogies are predominantly found as large, fault-bounded blocks in the northernmost massif. Pyroxene-bearing anorthositic mineralogies are predominantly constrained to the lower topographical regions of the SWPR, such as inside fresh craters and the graben walls.

A.4. Low-Albedo Features

Low-albedo features are areas where the surface is dark in NAC images, but no shadows are casting near or above the feature. To discover if any small-scale pyroclastic deposits exist in the SWPR area, we searched for dark mantling deposits (DMD; Mest 2011; Gustafson et al. 2012). First, NAC images with solar incidence angles of 60° – 80° were downloaded. NAC images with the lowest incidence angles showed fewer topographic and shadowing effects, which was ideal for

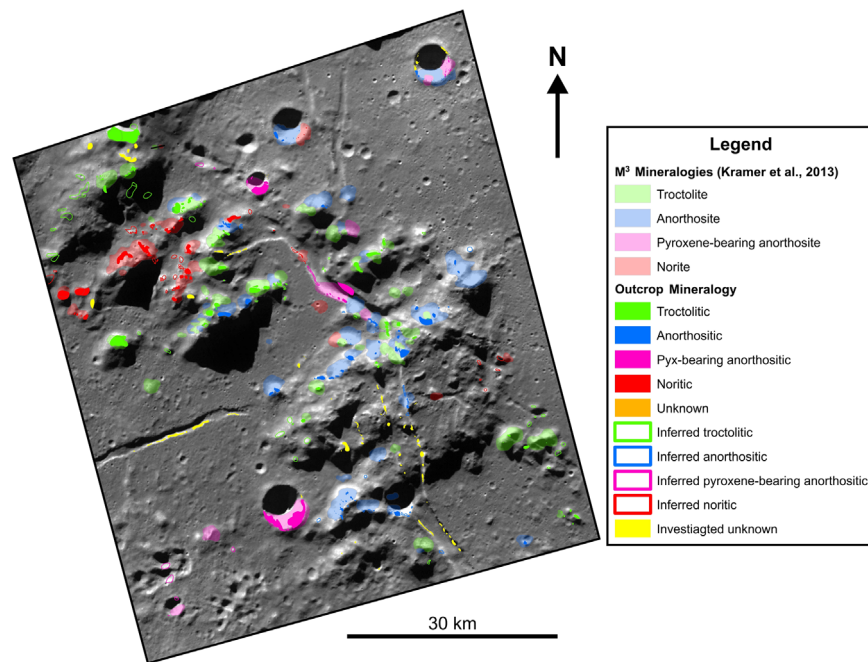


Figure A4. Mapped outcrops in the SWPR area, including inferred outcrops. Outcrops are distinguished as known (solid colors) and inferred (transparent colors). The outcrops are assigned mineralogies based on their position to M³ data (Kramer et al. 2013), topographic relationships, and albedo.

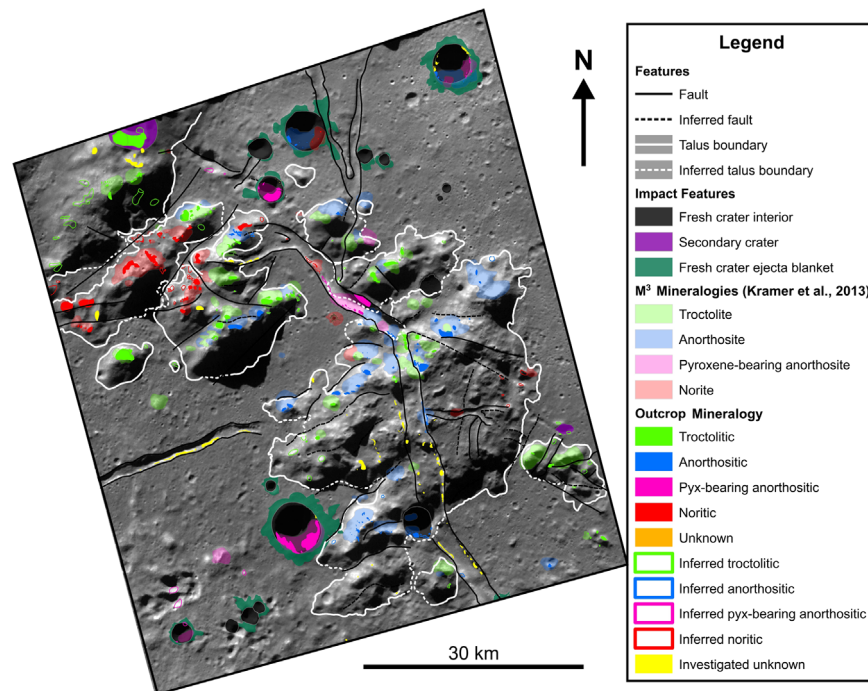


Figure A5. All features (faults, talus, fresh craters, crater ejecta, secondary craters, and outcrops) combined on a single map. The transparent polygons represent the M³ data coverage over the SWPR area (Kramer et al. 2013).

identifying these deposits. After a potential area was identified, we followed a checklist to determine if the feature should be noted as a potential DMD:

1. Material exhibits a smooth texture and does not contain large boulders in high-resolution images.
2. Material mantles and subdues subjacent terrain.
3. Deposit exhibits diffuse margins.
4. Material does not flood adjacent topographic lows.
5. Deposit surface does not exhibit lava flow textures.

6. Deposit occurs in association with rilles, fractures, or other possible vents.

If the feature met all of the criteria, then we examined additional NAC images of that area to determine if the low-albedo appearance was simply due to the area being shadowed. If the feature was still present in full illumination, then it was marked as a possible DMD by drawing a polygon around the edge of the DMD to best match its diffuse boundary.

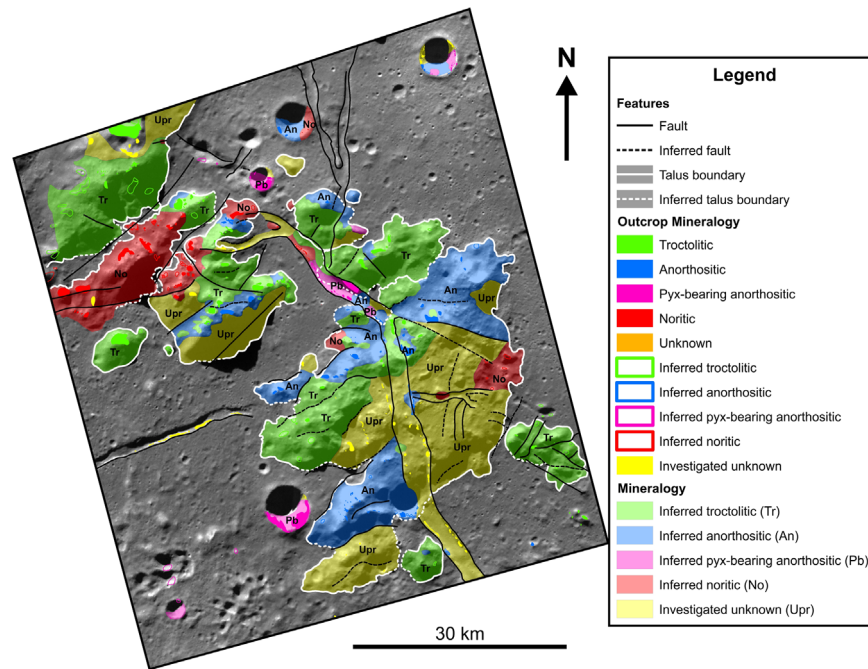


Figure A6. Map with mineralogies inferred over the entire peak-ring structure. The mineralogies were inferred using the location of M^3 signatures (Kramer et al. 2013), changes in albedo, and changes in topography. Mineralogical associations are labeled on the map.

Shapefiles for each feature and their metadata were compiled in ArcGIS. Each shapefile has assigned outcrop mineralogies, whether faults and grabens were known or inferred, the surface area of crater ejecta, and the boundaries of peak-ring talus material. The finished product overlays LRO WAC mosaics, the LOLA slope map, and LRO NAC images to complete the final geologic map.

Appendix B Traverse Planning

B.1. Identifying Features of Interest for Rover Exploration

All features of interest were marked on custom-shape layers in JMARS, using color-coded points and polygons (Figure B1). Potential traverse routes in this region are limited to a maximum slope of 15° to ensure rover mobility

(Potts et al. 2015; Steenstra et al. 2016; Bickel & Kring 2020). Subsequently, all features of interest are located on accessible slopes. To determine if the SWPR area is a viable region for a traverse, a LOLA slope map with a $29.63 \text{ m pixel}^{-1}$ resolution was overlaid onto the mapped region in JMARS. Data from all five sections were then combined into one file and uploaded to ArcGIS for ease of accessibility when reviewing sites for traverse planning.

B.2. Detailed Traverse Information

Tables B1–B3 provide detailed information for each station in Traverses A, B, and C, respectively. For each station, we provide location data, rock type (as inferred from M^3 data; see Kramer et al. 2013), and the type of sample we recommend. Figures B2 and B3 provide the LOLA slope context for the SWPR traverse area (resolution of 29.63 m/pixel).

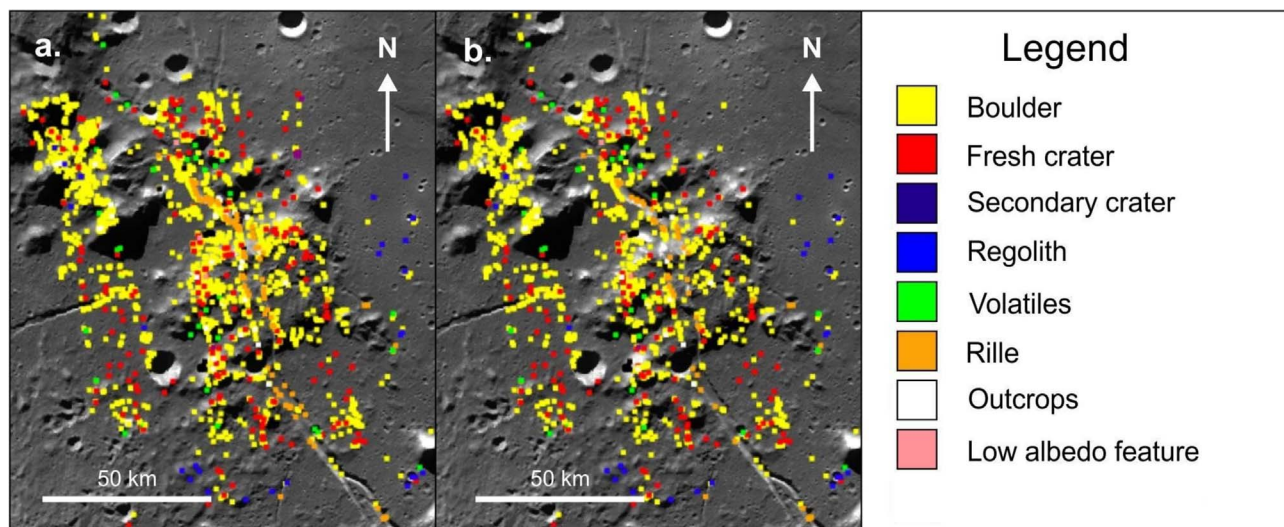


Figure B1. Points overlaid on a WAC mosaic of the SWPR showing FOI's marked on JMARS using custom-shape layers. The color-coding distinguishes the type of feature of interest: boulders (yellow), fresh craters (red), secondary crater (purple), regolith (blue), volatiles (green), rilles (orange), outcrops (white), and low-albedo features (pink).

Table B1
Details of Traverse A Stations

| Station | Latitude | Longitude | Elevation (m) | Slope (deg) | Distance from LS (m) | Surface Unit | M ³ Interpretation | Sample Type and Minimum Mass (kg) |
|---------|----------|-----------|---------------|-------------|----------------------|--------------|-------------------------------|-----------------------------------|
| LS | -75.54 | 126.72 | -8066 | 0.48 | 0 | Ish | n/a | Regolith/Rake: 2.0 |
| A1 | -75.58 | 127.01 | -7969 | 13.67 | 2642 | pNpr | Noritic | Crystalline Boulder: 0.5 |
| A2 | -75.58 | 127.27 | -7859 | 14.35 | 4795 | pNpr | Anorthositic | Crystalline Boulder: 0.5 |
| A3 | -75.52 | 127.58 | -7731 | 7.18 | 8275 | pNpr | Pyx-bearing Anorthositic | Crystalline Boulder: 0.5 |
| A4 | -75.53 | 127.38 | -7660 | 9.1 | 9970 | pNpr | n/a (Troctolitic) | Crystalline Boulder: 0.5 |
| A5 | -75.53 | 126.94 | -7918 | 6.93 | 14022 | pNpr | n/a | Regolith/Rake: 2.0 |
| A6 | -75.40 | 126.96 | -8068 | 0.6 | 18980 | Ish | Pyx-bearing Anorthositic | Crystalline Boulder: 0.5 |
| A7 | -75.45 | 126.76 | -8058 | 2.15 | 21927 | Ish | Noritic | Brecciated Boulder: 5.0 |
| A8 | -75.47 | 126.74 | -8075 | 0.93 | 22318 | Ish | Noritic | Brecciated Boulder: 5.0 |

Note. Surface units are derived from Kramer et al. (2013), Ish: smooth hummocky floor material; pNpr: peak-ring material.

Table B2
Details of Traverse B Stations

| Station | Latitude | Longitude | Elevation (m) | Slope (deg) | Distance from LS (m) | Lithological Unit | M ³ Interpretation | Sample Type and Minimum Mass (kg) |
|---------|----------|-----------|---------------|-------------|----------------------|-------------------|-------------------------------|-----------------------------------|
| LS | -75.54 | 126.72 | -8066 | 0.48 | 0 | Ish | n/a | Regolith/Rake: 2.0 |
| B1 | -75.58 | 127.01 | -7969 | 13.67 | 2642 | pNpr | Noritic | Crystalline Boulder: 0.5 |
| B2 | -75.57 | 127.10 | -7925 | 10.72 | 3318 | pNpr | Anorthositic/Noritic | Regolith/Rake: 2.0 |
| B3 | -75.58 | 127.27 | -7859 | 14.35 | 4784 | pNpr | Anorthositic | Crystalline Boulder: 0.5 |
| B4 | -75.53 | 126.94 | -7918 | 6.93 | 7774 | Ish | n/a | Regolith/Rake: 2.0 |
| B5 | -75.40 | 126.96 | -8068 | 0.6 | 12664 | Ish | Pyx-bearing Anorthositic | Crystalline Boulder: 0.5 |
| B6 | -75.45 | 126.76 | -8058 | 2.15 | 15611 | Ish | Noritic | Brecciated Boulder: 5.0 |
| B7 | -75.47 | 126.74 | -8075 | 0.93 | 16002 | Ish | Noritic | Brecciated Boulder: 5.0 |

Note. In situ analysis to be performed at each site. Surface units are derived from Kramer et al. (2013), Ish: smooth hummocky floor material; pNpr: peak-ring material.

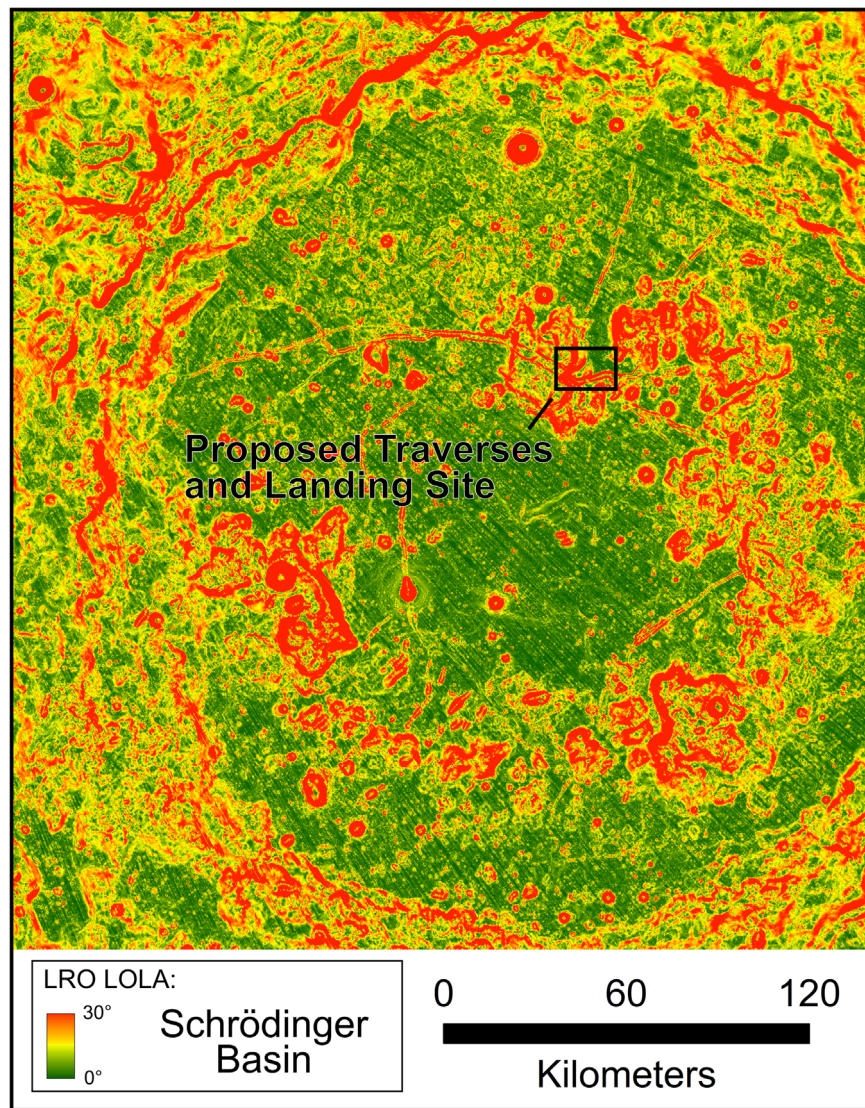


Figure B2. LRO LOLA slope map of the Schrödinger basin with a resolution of $29.63 \text{ m pixel}^{-1}$. The LOLA map was developed from a LOLA digital elevation model of the south pole.

Table B3
Details of Traverse C Stations

| Station | Latitude | Longitude | Elevation (m) | Slope (deg) | Distance from LS (m) | Lithological Unit | M ³ Interpretation | Sample Type and Minimum Mass (kg) |
|---------|----------|-----------|---------------|-------------|----------------------|-------------------|--|--|
| LS | -75.54 | 126.72 | -8066 | 0.48 | 0 | Ish | n/a | Regolith/Rake: 2.0 |
| C1 | -75.58 | 127.01 | -7969 | 13.67 | 2642 | pNpr | Noritic | Crystalline Boulder: 0.5 |
| C2 | -75.57 | 127.10 | -7925 | 10.72 | 3318 | pNpr | Anorthositic/Noritic | Regolith/Rake: 2.0 |
| C3 | -75.56 | 127.54 | -7859 | 14.35 | 4784 | pNpr | Anorthositic | Crystalline Boulder: 0.5 |
| C4 | -75.56 | 127.54 | -7818 | 2.25 | 6993 | pNpr | n/a | Regolith/Rake: 2.0 |
| C5 | -75.54 | 127.69 | -7772 | 6.9 | 8454 | pNpr | Anorthositic | Crystalline Boulder: 0.5 |
| C6 | -75.52 | 127.66 | -7913 | 9.64 | 9058 | pNpr | Anorthositic/Pyx-bearing Anorthositic | Regolith/Rake: 2.0 |
| C7 | -75.52 | 127.58 | -7731 | 7.18 | 9824 | pNpr | Pyx-bearing Anorthositic | Crystalline Boulder/ Regolith/Rake: 2.5 |
| C8 | -75.51 | 127.54 | -7707 | 7.09 | 10232 | pNpr | Pyx-bearing Anorthositic /Troctolitic | Regolith/Rake: 2.0 |
| C9 | -75.53 | 127.39 | -7660 | 9.1 | 11855 | pNpr | n/a (Troctolitic) | Crystalline Boulder: 0.5 |
| C10 | -75.53 | 126.94 | -7918 | 6.93 | 15907 | Ish | n/a | Regolith/Rake: 2.0 |

Note. Surface units are derived from Kramer et al. (2013), Ish: smooth hummocky floor material; pNpr: peak-ring material.

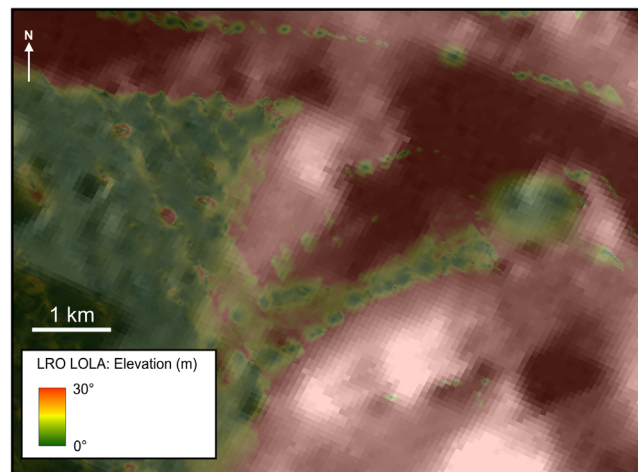


Figure B3. LRO LOLA slope map of the SWPR traverse region in JMARS with a resolution of $29.63 \text{ m pixel}^{-1}$.

B.3. Suggested Instrument Suite for a 14 Day Sample Return Mission in the SWPR Region

In this section, we present Table B4, which lists a notional instrument suite that could be included for the proposed traverses A, B, and C. The main focus of a proposed 14-day mission, as opposed to long-term missions, is the collection of samples. Therefore, in Table B4, two rover specifications are outlined. In the first scenario, the rover instrument suite is reduced to only the most essential instruments needed to

perform a traverse and collect samples (Table B4, above horizontal line). In this case, the time needed to perform only the most fundamental tasks at each station is 14.5 hours, which allows more time for traversing between stations and collecting samples. The second scenario outlines specifications for a rover that includes additional instruments designed for in situ analysis (Table B4, below the horizontal line). In this case, the time required at each station would increase to 19.5 hours (Table B4), which incorporates the time required for imaging, in situ analysis, and sample collection.

Table B4
Notional Instrument Suite for Proposed Traverses A, B, and C

| Instrument | Dimensions (cm) | Weight (kg) ^a | Power (W) ^a | Data Rate (kbps) |
|---|------------------------------------|--------------------------|------------------------|-------------------|
| Ground-penetrating radar (Mars 2020, RIMFAX) ^b | 20 × 12 × 7 | <3.90 | <13 | 5–10 |
| Microscope camera (MSL, MER) ^{c,d} | 8 × 8 × 10 | <0.4 | <0.4 | 8000 ^e |
| Surface imaging camera (MSL MastCam) ^f | 11 × 29 × 12 | <1.0 | <11.0 | 1.26 |
| Arm-mounted Alpha Particle X-Ray spectrometer (MSL, MER) ^{c,d} | 10.5 × 6 × 9 ^d | <2.20 | <7.3 | 18 |
| Gamma-ray spectrometer (JHU, APL) ^g | Sensor: 8 × 8 × 8 DPU: 10 × 15 × 5 | <1.82 | <3.25 | 0.01–0.1 |
| Neutron spectrometer (Resource Prospector) | ... | ... | ... | ... |

Note. The three instruments above the horizontal line are included on all traverses, those below are optional instruments only included for Traverse B. Optional payload includes in situ instrument specifications, which could be used if the mission timeline is extended.

^a 30% contingency included.

^b Hamran et al. (2016).

^c Arvidson & May (2010).

^d The proposed instrument is on board the MSL rover; however, values are from instruments flown on board the MER payload due to lack of data (Lakdawalla 2018). As the proposed instrument shares heritage with that on MER, the values are comparable.

^e Quoted as data rate before onboard processing.

^f Shearer & Tahu (2010).











^g Wieczorek et al. (2015).

B.4. List of NAC/WAC Images Used for SWPR Traverse

Here we provide a list of all NAC/WAC images used for planning of the SWPR traverses.

M156738805RC
M1098074615LC
M174483761LC
M174483761LC
M185017471LC
M189749586LC
M1105154228LC
M1105154228LC
M110779249LC
M115476987RC
M1115660849LC
M1115660849RC
M1118012077LC
M1118012077RC
M1131069667LC
M1131069667RC
M123736118LC
M123736118RC
M123742885LC
M123749687LC
M139084711RC
M167398258RC

ORCID iDs

E. C. Czaplinski  <https://orcid.org/0000-0002-2046-1416>
E. M. Harrington  <https://orcid.org/0000-0002-5218-8346>
S. K. Bell  <https://orcid.org/0000-0002-4638-2863>
G. D. Tolometti  <https://orcid.org/0000-0002-1900-2474>
B. E. Farrant  <https://orcid.org/0000-00031106-5785>
V. T. Bickel  <https://orcid.org/0000-0002-7914-2516>
C. I. Honniball  <https://orcid.org/0000-0001-8248-8991>
S. N. Martinez  <https://orcid.org/0000-0002-1812-5990>
H. M. Sargeant  <https://orcid.org/0000-0003-4987-5492>
D. A. Kring  <https://orcid.org/0000-0002-3440-6282>

References

- Arvidson, R. E., & May, L. 2010, Planetary Science Decadal Survey Mars 2018 MAX-C Caching Rover, <https://solarsystem.nasa.gov/studies/206/mars-2018-max-c-caching-rover/>
- Bickel, V. T., Honniball, C. I., Martinez, S. N., et al. 2019, *JGRE*, **124**, 1296
- Bickel, V. T., & Kring, D. A. 2020, *Icar*, **348**, 113850
- Bunte, M. K., Porter, S., & Robinson, M. S. 2011, in *Analogs for Planetary Exploration*, ed. W. B. Garry & J. E. Bleacher (Washington, DC: GSA), 533
- Burns, J. O., Mellinkoff, B., Spydell, M., et al. 2019, *AcAau*, **154**, 195
- Bussey, B., & Spudis, P. 2004, *The Clementine Atlas of the Moon* (Cambridge: Cambridge Univ. Press)
- Campbell, B. A. 2012, *JGRE*, **117**, E06008
- Carrier, W. D., Olhoeft, G. R., & Mendell, W. 1991, in *Physical Properties of the Lunar Surface*, ed. G. H. Heiken et al. (Cambridge: Cambridge Univ. Press), 475
- Carter, L. M., Neish, C. D., Bussey, D. B. J., et al. 2012, *JGRE*, **117**, E00H09
- Christensen, P. R., Engle, E., Anwar, S., et al. 2009, *AGUFM*, **IN22A-06**
- Costes, N. C., George, E. B., & Farmer, J. E. 1972, *Mobility Performance of the Lunar Roving Vehicle: Terrestrial Studies—Apollo 15 Results* (Washington, D.C: NASA), <https://core.ac.uk/display/63219706>
- Dence, M. R., Grieve, R. A. F., & Robertson, P. B. 1977, in *Proc. of the Symp. on Planetary Cratering Mechanics, Impact and Explosion Cratering: Planetary and Terrestrial Implications* (New York: Pergamon Press), 247
- Dymek, R. F., Albee, A. L., & Chodos, A. A. 1975, *LPSC*, **1**, 301
- Fortezzo, C. M., Spudis, P. D., & Harrel, S. L. 2020, *LPSC*, **51**, 2760
- Green, R. O., Pieters, C., Mouroullis, P., et al. 2011, *JGRE*, **116**, E00G19
- Gustafson, J. O., Iii, J. F. B., Gaddis, L. R., Hawke, B. R., & Giguere, T. A. 2012, *JGRE*, **117**, E00H25
- Hamran, S.-E., Amundsen, H. E. F., Asak, L., et al. 2016, in *3rd Int. Workshop on Instrumentation for Planetary Missions* (Pasadena, CA), 4031
- Heiken, G., Vaniman, D., & French, B. M. 1991, *Lunar Sourcebook: A User's Guide to the Moon* (Cambridge: Cambridge Univ. Press)
- Hiesinger, H., Landgraf, M., Carey, W., et al. 2019, *LPSC*, **50**, 1327
- Honniball, C. I., Lucey, P. G., Li, S., et al. 2021, *NatAs*, **5**, 121
- Hufenbach, B., Laurini, K. C., Satoh, N., et al. 2015, in *66th Int. Astronautics Congress, International Missions to Lunar Vicinity and Surface-Near-Term Mission Scenario of the Global Space Exploration Roadmap* (Jerusalem), 1
- Hurwitz, D., & Kring, D. A. 2015, *E&PSL*, **427**, 31
- IASIS 2018, *International Deep Space Interoperability Standards—Draft C*, <https://www.internationaldeepspacestandards.com/wp-content/uploads/sites/45/2018/03/Combined-Draft-C-February-2018.pdf>
- International Space Exploration Coordination Group 2018, *The Global Exploration Roadmap*, https://www.nasa.gov/sites/default/files/atoms/files/ger_2018_small_mobile.pdf
- Jozwiak, L. M., Head, J. W., & Wilson, L. 2015, *Icar*, **248**, 424
- Klimczak, C. 2014, *Geo*, **42**, 963

- Kramer, G. Y., Kring, D. A., Nahm, A. L., & Pieters, C. M. 2013, *Icar*, **223**, 131
- Kring, D. A., Claeys, P., Gulick, S. P. S., et al. 2017, *GSA Today*, **27**, 4
- Kring, D. A., & Durda, D. D. 2012, A Global Lunar Landing Site Study to Provide the Scientific Context for Exploration of the Moon, <https://www.lpi.usra.edu/exploration/CLSE-landing-site-study/>
- Kring, D. A., Kramer, G. Y., Collins, G. S., Potter, R. W. K., & Chandnani, M. 2016, *NatCo*, **7**, 13161
- Kumar, P. S., Keerthi, V., Senthil Kumar, A., et al. 2013, *JGRE*, **118**, 206
- Kumar, S. P., Sruthi, U., Krishna, N., et al. 2016, *JGRE*, **121**, 147
- Lakdawalla, E. 2018, *The Design and Engineering of Curiosity* (Chichester: Springer),
- Landgraf, M., Carpenter, J., Sawada, H., Agency, E. S., & Elements, A. 2015, in Annual Meeting of the Lunar Exploration Analysis Group (Columbia, MD), **2039**
- Li, S., Lucey, P. G., Milliken, R. E., et al. 2018, *PNAS*, **115**, 8907
- Loflin, K., Captain, J., Griffin, T., et al. 2013, in 9th Workshop on Harsh-Environment Mass Spectrometry, Integration and Ruggedization of a Commercially Available Gas Chromatograph and Mass Spectrometer (GCMS) for the Resource Prospector Mission (RPM) (St. Petersburg, FL), 1
- Mest, S. C. 2011, in Recent Advances and Current Research Issues in Lunar Stratigraphy, Vol. 477, ed. W. A. Ambrose & D. A. Williams (Washington, DC: GSA), 95
- National Research Council 2007, in *The Scientific Context for Exploration of the Moon* (Washington, DC: National Academies Press), <https://www.nap.edu/catalog/11954/the-scientific-context-for-exploration-of-the-moon>
- Neish, C. D., Hamilton, C. W., Hughes, S. S., et al. 2017, *Icar*, **281**, 73
- Nozette, S., Spudis, P., Bussey, B., et al. 2010, *SSRv*, **150**, 285
- Ohtake, M., Haruyama, J., Matsunaga, T., et al. 2008, *EP&S*, **60**, 257
- O'Sullivan, K. M. O., Thaisen, K. G., & Kring, D. A. 2011, *Geol Soc Am*, **2477**, 117
- Pernet-Fisher, J., & Joy, K. 2016, *A&G*, **57**, 1.26
- Potts, N. J., Gullikson, A. L., Curran, N. M., et al. 2015, *AdSpR*, **55**, 1241
- Prinz, M., & Keil, K. 1977, *PCE*, **10**, 215
- Research Team, K. L., & Kramer, G. 2014, *Icar*, **228**, 141
- Robinson, M. S., Brylow, S. M., Tschimmel, M., et al. 2010, *SSRv*, **150**, 81
- Sargeant, H. M., Bickel, V. T., Honniball, C. I., et al. 2020, *JGRE*, **125**, e06157
- Schultz, P. H. 1976, *Moon*, **15**, 241
- Seeni, A., Schfer, B., & Hirzinger, G. 2010, *Aerosp Technol Adv.*, doi:10.5772/6930
- Shearer, C., & Tahu, G. 2010, Lunar Polar Volatiles Explorer (LPVE) Mission Concept Study, <https://solarsystem.nasa.gov/studies/204/lunar-polar-volatiles-explorer-lpve-mission-concept-study/>
- Shih, C. Y., Nyquist, L. E., Dasch, E. J., et al. 1993, *GeCoA*, **57**, 915
- Shoemaker, E. M., Robinson, M. S., & Eliason, E. M. 1994, *Sci*, **266**, 1851
- Smith, D. E., Zuber, M. T., Jackson, G. B., et al. 2010, *SSRv*, **150**, 209
- Steenstra, E. S., Martin, D. J. P., McDonald, F. E., et al. 2016, *AdSpR*, **58**, 1050
- Stöffler, D., Knöll, H.-D., Marvin, U. B., Simonds, C. H., & Warren, P. H. 1980, *Lunar Highlands Crust* (New York: Pergamon Press), **51**
- Wieczorek, M., Mimoun, D., Baratoux, D., et al. 2015, *FARSIDE: A Mission to the Farside of the Moon*, Nission Concept Report
- Wilhelms, D. E., Howard, K. A., & Wilshire, H. G. 1979, *US Geol Surv.*, **1**, 1162
- Wood, J. A., Dickey, J. S., Marvin, U. B., & Powell, B. N. 1970, *Sci*, **167**, 602
- Xu, X., Hui, H., Chen, W., et al. 2020, *E&PSL*, **536**, 116138